INVESTIGATION OF MAGNETIC BISTABILITY FOR A WIDER BANDWIDTH IN VIBRO-IMPACT TRIBOELECTRIC ENERGY HARVESTERS

by

QAIS QASEEM

A thesis submitted in partial fulfillment of the
requirements for the degree of
Master of Science in Mechanical Engineering
Department of Mechanical Engineering

Alwathiqbellah Ibrahim, Ph.D., Committee Chair

College of Engineering

The University of Texas at Tyler
March 2023

The University of Texas at Tyler
Tyler, Texas

This is to certify that the Master's Thesis of

QAIS QASEEM

has been approved for the thesis requirement on

09 March 2023

For the Master of Science in Mechanical Engineering

Approvals:

DocuSigned by:
Alwathiqbellah Ibrahim
3A3F3DF38EA844C...
Thesis Chair: Alwathiqbellah Ibrahim, Ph.D.

DocuSigned by:
Nael Barakat
30D27AF79E60404...
Member: Neal Barakat, Ph.D.

DocuSigned by:
Nelson Fumo
9BAB5E76B5E14AE...
Member: Nelson Fumo, Ph.D.

DocuSigned by:
Talisin Khayali
ACA7690059AD419...
Chair, Department of Mechanical Engineering

DocuSigned by:
3E50E32BE8F046A...
Dean, College of Engineering

Acknowledgments

First and foremost, I want to give God, Most Gracious, Most Merciful, all the praise and gratitude for his gifts that have given me the endurance, serenity, and good health to complete this task.

I would like to convey my sincere gratitude and appreciation to Dr. Alwathiqbellah Ibrahim, my academic adviser, for his ongoing support and guidance, as well as for his amazing demeanor in providing assistance with care and patience. I owe a great deal to Dr. Nael Barakat for his direction and continual watchfulness since the first day I arrived at the University of Texas at Tyler. I want to express my gratitude to Dr. Nelson Fumo for all the knowledge he has imparted to me; I have gained a lot from him.

I want to thank everyone for their great support, which enabled me to complete this thesis. Atmeh, Mostafa, Hadeel, and Katy were interesting lab partners. I want to thank you all for the thought-provoking conversations, the long nights of work, and the enjoyable times we shared. My coworkers and others who have voluntarily assisted me are Mohammad, Rami, Sufian, Mustafa, and Habeb. Last but not least, I want to acknowledge my family, especially my parents, Husam, Reema, Qusai, and Ameer, for their support and encouragement in getting me through this project. In addition, Salah, Ghassan, and Husam, my uncles, are constantly encouraging. Thanks to everybody!

Table of Contents

List of Tables

List of Figures

Abstract

Mechanical energy from vibrations is widespread in the ambient environment. It may be harvested efficiently using triboelectric generators. Nevertheless, the harvesters' effectiveness is restricted because of the limited bandwidth. This thesis proposed a comprehensive theoretical and experimental investigation of a variable frequency energy harvester, which integrates a Vibro-impact triboelectric-based harvester and magnetic nonlinearity to increase the operation bandwidth and improve the efficiency of conventional triboelectric harvesters. A cantilever beam with a tip magnet is aligned with another fixed magnet at the same polarity to induce a nonlinear magnetic repulsive force. A triboelectric harvester is integrated into the system by utilizing the lower surface of the tip magnet to serve as the top electrode of the harvester, while the bottom electrode with an attached Polydimethylsiloxane insulator is placed underneath. Numerical simulations are performed to examine the impact of the potential wells formed by the magnets. The structure's static and dynamic behavior at varying excitation levels, separation distance, and surface charge density are all discussed. In order to develop a variable frequency system with wide bandwidth, the system's natural frequency varies by changing the distance between the two magnets to reduce or magnify the magnetic force to

achieve monostable or bistable oscillations. When the system is excited by vibrations, the beams will vibrate, which will cause an impact between the triboelectric layers. This impact will produce an alternating electrical signal through periodic contact-separation motions between the harvester's electrodes. Theoretical findings were experimentally validated. The findings of this research have the potential to pave the way for developing an effective energy harvester capable of scavenging energy from ambient vibrations across a broad range of excitation frequencies. We enhanced the frequency bandwidth by 110.41 % compared to the conventional energy harvester. Combining magnetic nonlinearity and Vibro-impact can effectively broaden the operational frequency bandwidth and enhance the harvested energy for triboelectric energy harvesters.

Chapter One

Introduction and Literature Review

Mechanical vibrations, such as human motions, cars, and equipment, are significant sources of lost mechanical power in our daily environment [1–3]. Therefore it is one of the most frequent forms of wasted energy that can be converted into environmentally renewable energy that could be used to power widely used microelectronics in environment control, emergency response, monitoring and control of industrial processes, health monitoring of aircraft, ships, automobiles, and drilling rigs, and many other applications [4–16]. The frequency bandwidth of environmental vibration energy is vast, with low-frequency components dominating [17]. Consequently, the thought of harnessing such ambient energy is enticing [18].

Recently, energy harvesting presented as a novel solution for converting wasted energy into usable electrical energy because of the advantages of being environmentally friendly and minimal maintenance costs compared to batteries as a power source. However, the currently proposed vibration energy harvesting systems still suffer from the narrow operational bandwidth

[19, 20]. Multiple transduction systems have been employed to transform wasted mechanical energy into useable electricity such as electromagnetic [21–23], piezoelectric [24–26], electrostatic [27–29] and triboelectric [30–34]. With low-cost materials, high power density, environmental friendliness, extended service life, and simple fabrication, triboelectric energy harvesting is considered an efficient method for converting small-scale kinetic energy into electricity [35]. In addition, the triboelectric energy harvesting technique has widespread applications utilizing many vibration sources, such as human activities [36–38], wind flow [39–41], and mechanical vibration [31, 42, 43]. The working principle of triboelectricity is based on electrification, and electrostatic induction, which happens when two materials with opposite polarities come into contact and then separate [44–46].

Even though the external environmental excitations have a broad range, the linear vibration energy harvesters have a narrow frequency bandwidth which minimizes the amount of energy that can be harvested. Therefore, these harvesters must only be activated at resonance frequency to achieve a satisfactory energy conversion rate Small deviations in external excitation frequency from the resonance frequency of a linear vibration energy harvester substantially impact its performance, which makes them inefficient. In reality, by expanding the frequency bandwidth of a harvester, the system can be more effective across a broader spectrum of external frequencies [47, 48]. Adding nonlinearity to the system is one of

the most appropriate strategies for enhancing the frequency bandwidth of a harvester [49, 50]. Several techniques for exploiting nonlinearity have been studied, including duffing [51–54], impact [55–60], and bistable oscillator designs [61–63]. Recently, Vibro-impact has been applied to vibration energy harvesters to boost harvesting efficiency. Numerous technical applications use Vibro-impact, including cutting and grinding equipment, pile-driving machines, turbomachinery, frequent rubbing of the rotor blades and stators, and hand-held percussion devices [64]. Several studies investigated triboelectric and electrostatic effects utilizing Vibro-impact structures and achieved higher bandwidth compared to the non-impact harvesters [65]. The Vibro-impact of multidegrees of freedom systems increased the operational bandwidth [59,66–71]. However, such systems need to be bulky and fabricated in large sizes. Other techniques were used to increase the output power, and operating frequency bandwidth of piezoelectric and triboelectric energy harvester devices, such as mechanical impact [59, 60, 72], and mechanical stoppers [67, 73, 74]. However, all these previous studies have a specific range for operating frequencies, and changing the operating range requires modifying the structural parameters. Nonlinearities are another approach to extending the operating bandwidth of energy harvesters via bistability [43, 63, 75–77], compared to linear harvesters. However, the enhancement in the operating bandwidth utilizing only nonlinearity is still insignificant.

Nonlinearity played a significant role in expanding the bandwidth of linear harvesters. Structural and magnetic nonlinearities are some of the most common techniques that are often used to increase frequency bandwidth, and harvesting efficiency [78]. Scientists have devised numerous designs to produce bistable conditions, which broadens the response bandwidth and boosts the harvesting efficiency [79, 80]. For example, a cantilever beam structure with two magnets generates monostable and bistable potential energy depending on the magnetic spacing fluctuation [63, 77]. Nonlinear hysteresis (softening, hardening) induced large amplitude oscillations that significantly expanded the frequency bandwidth for both monostable [81] and bistable harvesters [82]. In addition, the interwell motions due to the high kinetic energy in bistable energy harvester systems broadened the frequency bandwidth and enhanced the average power density [83]. Such bistable systems have been extensively explored and widely implemented in piezoelectric [84] and magnetoelectric energy harvesting [21], and electromagnetic energy harvesters [85]. A bistable actuator coupled with a flexible triboelectric nanogenerator sensor to detect bladder fullness and help to empty it [86]. The work used permanent magnets and springs as a bistable structure in a TEH for broadband energy harvesting at low frequencies [87]. However, these studies in triboelectric didn't shed light on the dynamic behavior of the harvesters, and in general, there is a lack of investigation into the static and dynamic behaviors of the bistable triboelectric energy harvesting systems.

In this study, we presented a variable frequency nonlinear Vibro-impact energy harvester based on triboelectric with induced magnetic nonlinearity under harmonic excitations to increase the bandwidth. We contributed by combining magnetic nonlinearity with Vibro-impact to enhance the operating bandwidth of the linear Vibro-impact harvesters. We developed a theoretical lumped piecewise model to comprehend the harvester's static and dynamic behaviors. We experimentally validated our model to prove the viability of adding magnetic nonlinearity to the triboelectric transduction mechanism. This article is structured as follows: The design and configurations of triboelectric energy harvesters are covered in the Configuration section. We constructed the theoretical model utilizing a lumped parameter model technique in the model part, and the findings and discussion section provided the associated results that were experimentally validated. In the conclusion section, we wrap up by drawing some conclusions.

Chapter Two

Thesis Overview

The main objective of this chapter is to provide an overview of the subjects that were investigated for this study. To this end, each topic's issue description, methodology, and contribution were established and made clear. This study's main objective is to increase the effectiveness of triboelectric energy harvesters by broadening the bandwidth using a combination of nonlinear magnetic force and nonlinear impact.

A Triboelectric Energy Harvester with Impact for Larger Bandwidth

Problem Statement

In triboelectric energy harvesting, the narrow bandwidth of the linear harvester is one of the major drawbacks that result in a low amount of energy being harvested which limits its effectiveness. Therefore, the overlapping between the operational bandwidth of the energy harvesters and the ambient vibrations should be maximized to increase the amount of energy being harvested. This study will address and overcome the narrow bandwidth limitation by combining magnetic nonlinearity and Vibro-impact to improve the harvesting bandwidth of triboelectric energy harvesters.

Methodology

We combine magnetic nonlinearity and Vibro impact for bandwidth improvement in triboelectric energy harvesters. A combined mechanism was proposed using a SDOF Cantilever Beam System with an integrated magnates and triboelectric energy harvester. For wideband energy harvesting, the triboelectric generator will serve as an electrical generator and a mechanical stopper. A theoretical lumped parameter model is built to investigate the system's dynamic behavior and the electrical signal produced. The system of the governing

equations is numerically solved using the Long-Time Integration (LTI) technique [88]. The simulation's findings will make it possible to pinpoint variables and elements that impact how well the harvester works. The experimental setup utilized a closed-loop control circuit. The system consists of an amplifier that amplifies the signal from the controller to power an electrodynamics shaker, which is used to apply regulated vibrations to the harvester, and a vibration research controller that controls the range of excitation frequencies as well as the excitation intensity. Experimental verification and confirmation of the simulated results were carried out by running this setup at various excitation levels and recording the resulting data.

Contribution

This study is unique in that it combines magnetic nonlinearity with Vibro-impact to increase the harvesting bandwidth of triboelectric energy harvesters. The combination of magnetic nonlinearity and Vibro-impact is a novel strategy for triboelectric energy harvesters applications. It has never been investigated in the literature.

Chapter Three

A Nonlinear Triboelectric Energy Harvester with Impact for Larger Bandwidth

Magnetic Vibro-Impact

In this chapter, the dynamic model and the performance of a triboelectric cantilever-based Vibro-impact energy harvester under base excitation will be investigated. This work is similar to [63], but under the contribution of the triboelectric transduction mechanism. The harvester consists of a cantilever beam attached to a tip magnet aligned with another fixed magnet at the same polarity to induce a nonlinear magnetic repulsive force. An Aluminum electrode is connected to the tip mass to create the upper electrode of the triboelectric generator. Another Aluminum electrode with bonded PDMS insulator is attached to the fixed base (holding the whole structure) and acts as a lower electrode and mechanical stopper. Under base excitation, the system vibrates and leads to a contact-separation motion between the two electrodes, generating a wide-band AC electrical signal.

The proposed harvester is fit for various low-frequency operation conditions because it has a relatively wide bandwidth resulting from combining magnetic nonlinearity with Vibro-impact. Targeting an ultimate wide-band response that is investigated from the combination is one of the main goals of this study. Towards this, different setups, configurations, and parameters will be investigated to eliminate the narrow bandwidth limitation of the linear vibration energy harvesters.

Device Design and Configuration

A permanent magnet is attached to the tip of a cantilever beam. Another fixed magnet faces the tip magnet at the same polarity to induce magnetic nonlinearity to the structure. An Aluminum layer is attached to the bottom surface of the tip magnet and serves as an upper electrode of the triboelectric energy harvester. Another Aluminum layer coated with Polydimethylsiloxane (PDMS) is fixed below the upper electrode and acts as the lower electrode of the triboelectric generator. A schematic of the whole structure is shown in Fig. 3.1. When the structure is subjected to a base excitation, the cantilever beam vibrates, and the two electrodes will contact each other periodically, generating an electrical signal. The two magnets are separated by a distance d, which determines the nature of the oscillations. At large d, the magnetic force is weak, and the system oscillates around a single

well, known as mono-stable oscillation. In contrast, at low d, the magnetic force magnified the system oscillates in a double well, known as Bi-stable oscillations.

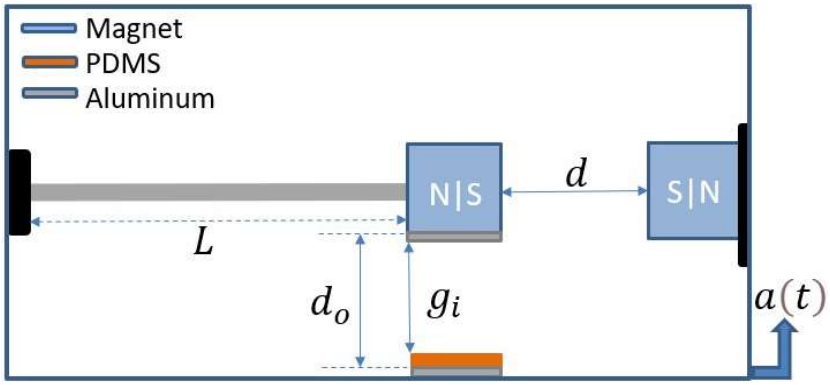

Figure 3.1. Schematic of the nonlinear energy harvester under base excitation.

The principle of operation for the nonlinear harvester is shown in Fig. 3.2. The stability of the harvester is a function of the distance between the two magnets, Fig. 3.2a. The repulsive magnetic force becomes weak when the two magnets are set far from each other (large d), and the beam oscillates at a single stable equilibrium point around its horizontal axis, case 1 in Fig. 3.2a, and this is called monostable range. The corresponding potential energy function is shown in Fig. 3.2b at a separation distance of $d > 9$, where a single potential well profile is shown and reflects the oscillation around case1 in Fig. 3.2a. In contrast, when the distance between the two magnets is set close to each other (small d), the repulsive magnetic force becomes strong and forces the beam to oscillate at double stable equilibrium points around its horizontal axis, cases 2 and 3 in Fig. 3.2a, and this is called bistable range. The

corresponding potential energy function is shown in Fig. 3.2b at a separation distance of $d < 9$, where double potential well profiles are shown and reflect the oscillation around cases 2 and 3 in Fig. 3.2a. From Fig. 3.2b, we can see that oscillations of the system are transferred from a single potential well to a double potential well by lowering the distance between the two magnets. Furthermore, the barrier between the double-potential wells becomes higher compared to the system's energy, and then there are two degenerate states corresponding to the energy being localized in one or the other of the wells.

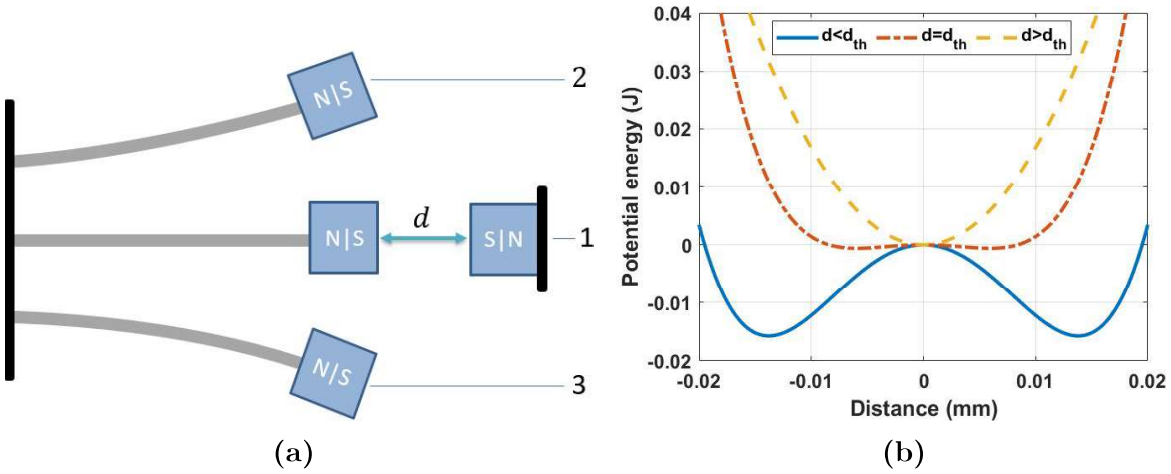

Figure 3.2. The principle of operation of the nonlinear harvester as a function of the distances between two magnets (a) Stability, (b) Potential energy.

The triboelectric generator consists of two layers with opposing electron loss and gain tendencies and generates electricity through periodic contact and separation between the harvester's electrodes via contact electrification and electrostatic induction. The detailed working mechanism of the triboelectric generator is depicted in Fig. 3.3. Initially, the

harvester's electrodes are neutral and free of charge. When the base excitation is strong enough to overcome the restoring force from the elastic beam, the harvester's electrodes will come into contact, the upper Al layer will become positively charged, and the PDMS layer will be negatively charged. Then, when the base excitation is weak, the restoring force from the elastic beam will dominate, forcing the harvester's electrodes to separate from each other, and the current will flow from the upper Al layer to the lower one due to the potential difference between them. Once the electrostatic and triboelectric charges are liberated, they equalize and reach equilibrium. However, when the mechanical load is applied again, it will break the equilibrium, capacitance is charged, and current flows in the opposite direction resulting in an alternating current being generated. For further details on the triboelectric phenomenon, a reader can refer to [12]. The PDMS layer also works as a mechanical stopper restricting the deflection of the Secondary beam, which introduces the piecewise linearity to the system, resulting in a broadband of the proposed harvester [89–91].

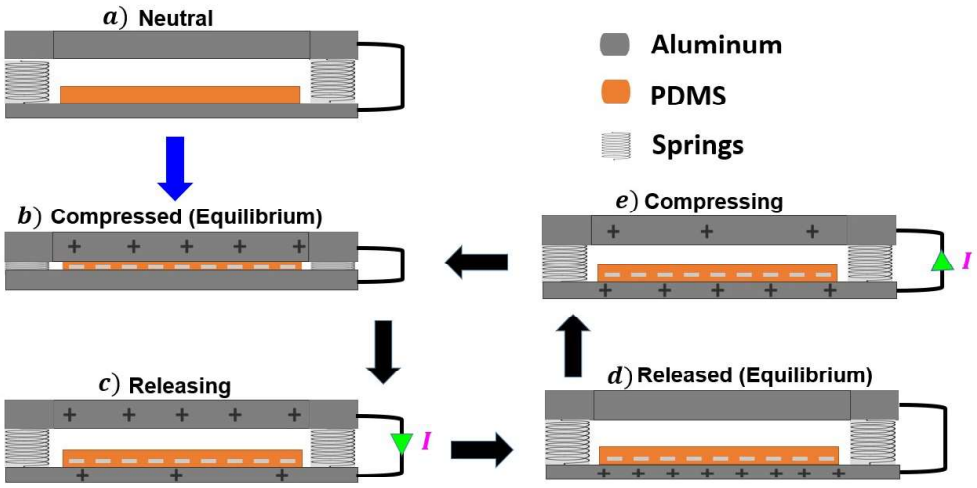

Figure 3.3. Triboelectric energy harvester cycle of work.

Theoretical Model

A lumped parameter model of a SDOF system is used to simulate the dynamic behavior and the generated electrical system. When the tip magnet faces another fixed magnet at the same polarity in the Vibro-impact energy harvester, a repulsive magnetic force will be induced between the two magnets. The total repulsive magnetic force (F_{mag}) is a function of the deflection of the beam, y, and the horizontal distance between the two magnets, d, and can be decomposed into horizontal and vertical components, Fig. 3.4. For simplicity, the horizontal component (F_{magx}) will be neglected with the assumption that it is equivalent to the longitudinal stiffness of the cantilever beam. However, the vertical component (F_{magy}) will be dominant and affect the transverse deflection of the cantilever beam.

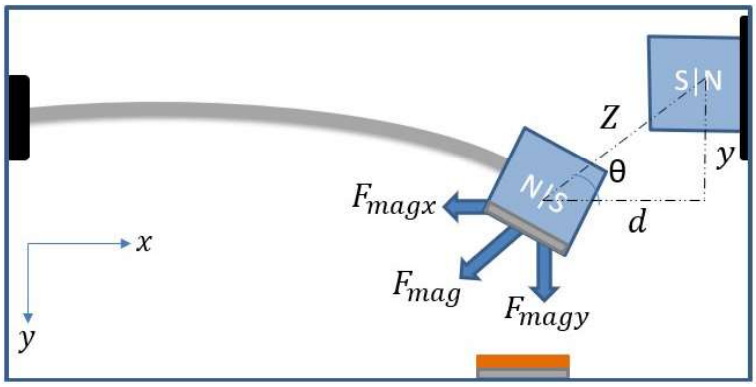

Figure 3.4. Schematic for the total magnetic force acting on tip magnets.

The total magnetic force acting on both magnets is given by Eqn. 3.1. Where Z is the distance between the two magnets' centers and given by: $(Z = \sqrt{d^2 + y^2})$, Further, F_R is the size of the magnetic dipole moments and given by ($F_R = \frac{3\epsilon q_1 q_2}{2\pi}$), where q_1 and q_2 are the magnetic dipole moments for the two magnets. Using the angle θ, the vertical component (F_{magy}) will be given by Eqn. (3.2). Where μ is the permeability of the space and it equals $4\pi \times 10^{-7}\ mkg/s^2A^2$.

$$F_{mag} = \frac{F_R}{Z^4} \tag{3.1}$$

$$F_{magy} = \frac{F_R y}{(d^2 + y^2)^{5/2}} \tag{3.2}$$

To investigate the static and dynamic behavior of the nonlinear harvester, we modeled the structure as a Single Degree of Freedom (SDOF) lumped parameter system as shown in Fig. 3.5. The upper electrode of the triboelectric harvester is attached to the bottom of the lumped mass and separated by an initial gap g_i from the PDMS layer attached to the lower fixed electrode. Under base excitations, there will be two motion scenarios: non-impact and impact. The non-impact scenario occurs when the deflection of the upper electrode is less than the initial gap, as illustrated in Fig. 3.5a. When the deflection is larger than or equal to the initial gap, the upper Al electrode will be in contact with the PDMS and start penetrating to reflect the impact scenario, as illustrated in Fig. 3.5b. After the impact, the system becomes stiffer and more damped, which is introduced to the system by the additional impact stiffness k_i and impact damping c_i.

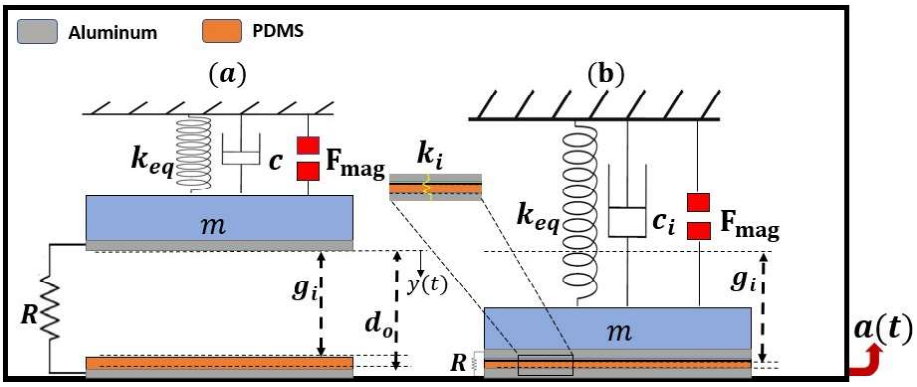

Figure 3.5. Single degree-of-freedom vibration system before impact and at the start of the impact.

The theoretical governing equation can be extracted from the free body diagrams for the SDOF shown in Fig. 3.5 with all forces acting on the lower electrode for the non-impact and impact scenarios. Following the procedure presented in [60], the piece-wise governing equations for the non-impact and impact scenarios were extracted and shown in Eqn. (3.3). The two electrodes of the triboelectric energy harvester will serve as a parallel plate capacitor, and the third equation in Eqn. (3.3) represents the electrical domain equation responsible for electrical signal generation. The term m is the equivalent mass of the beam, and k_{eq} is the equivalent stiffness of the cantilever beam with the mass of the tip and given by $k_{eq} = \frac{3EI}{L^3}$ [92]. The electrostatic force of the capacitor and can be expressed as [93, 94] is given by $F_e = \frac{q^2(t)}{2\epsilon_0 \epsilon_r S}$, where $q(t)$ is the number of charges carried between two electrodes, S is the entire surface area of contact, ϵ_r is the dielectric constant of the PDMS, and ϵ_0 is the vacuum permittivity. The term $a(t)$ represents the harmonic base excitation and is equal to

$a(t) = A\ cos(\Omega\ t)$, where A is the amplitude, and Ω is the excitation frequency. Moreover, c_i and k_i indicate the coefficients of impact damping and stiffening, respectively. Also, g_i is the distance between the upper electrode and the PDMS surface, wherein d_0 represents the distance between the two Al electrodes. The terms σ, T, and R represent the surface charge density, PDMS thickness, and external resistance. The rest of the parameters used in this study are listed in Table 4.1. Next, the governing equations can be solved numerically to examine the dynamic behavior of the system and the generated electrical signal.

$$\begin{cases} m\ddot{y} + c\dot{y} + k_{eq}y - F_{magy} + F_e = ma, & y(t) < g_i \\ m\ddot{y} + c_i\dot{y} + k_{eq}y + k_i(y(t) - g_i) - F_{magy} = ma, & y(t) \geqslant g_i \end{cases}. \tag{3.3}$$

$$\dot{q} = -\frac{q(t)}{\epsilon_0 RS}\left(\frac{T}{\epsilon_r} + d_0 - y(t)\right) + \frac{\sigma}{\epsilon_0 RS}(d_0 - y(t))$$

Experimental Validation

SOLIDWORKS is used to design and assemble the harvester construction as a CAD model. comprising a base and mountings, aluminum beam with proof mass, and triboelectric generator

as its three primary components. A 3D printer is used to manufacture the base and mountings. Then, every component was put together.

To validate our theoretical model, the experimental setup shown in Fig. 3.6 is used to test the static and dynamic behaviors of the nonlinear harvester. The arrangement consists of a $VR9500$ controller, amplifier, and electrodynamics shaker with a mounted nonlinear energy harvester structure. The control unit regulates the base excitation applied by the shaker to control the amplitude and frequency. The control unit sends the signal to the amplifier for amplification to the required level to be sent to the shaker that transfers the base excitations to the harvester. An accelerometer is attached to the cantilever beam's tip mass to record deflections in response to sweeping excitation frequencies. In addition, the voltage generated by the triboelectric generator is measured by the controller.

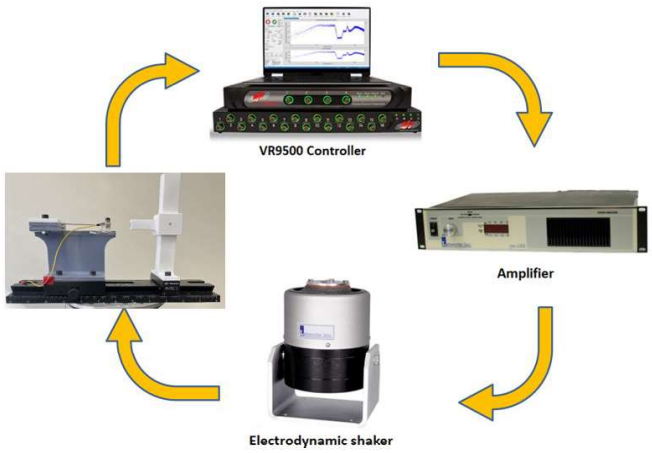

Figure 3.6. The experimental setup used for testing the triboelectric energy harvester.

Results and Discussion

In this section, the system is numerically solved and experimentally validated to facilitate further analysis, identify the crucial elements that will lead to a more effective energy harvester, and examine the potential for energy scavenging in the proposed harvester. Towards this, the physical and geometrical parameters given in Table. 4.1 are used.

Table 3.1. Physical and geometrical parameters to be used in the model.

Parameters	**Symbol**	**Value**
Beam ($length \times width \times thickness$)	$L \times b \times h$	$(75 \times 10 \times 1)$ mm
Beam Young's modulus	E	69 Gpa
Beam density	ρ	2700 kg/m^3
Impact damping coefficient	c_i	3.2 c N.s/m
Impact stiffness coefficient	k_i	3.2 k_{eq} N/M
PDMS layer thickness	T	1×10^{-3} m
Resistance	R	10 MΩ
Magnets side length	L_m	8.0 mm
Magnetic moment	$q_1 = q_2$	0.5 A$^2/m$
PDMS ($length \times width \times thickness$)	$L_p \times b_p \times h_p$	$(20 \times 20 \times 1)$ mm
PDMS vacuum permittivity	ϵ_0	8.854×10^{-12}

Static Analysis

The static deflection of the beam is a function of the distance between the two magnets due to the repulsive magnetic force. By setting all the time derivatives to zero in Eq. (3.3), the static governing equation can be given by:

$$ky_s - F_{magys} = 0 \tag{3.4}$$

Where

$$F_{magys} = \frac{F_R y_s}{(d^2 + y_s^2)^{5/2}} \tag{3.5}$$

Where y_s represents the static deflection of the cantilever beam, and F_{magys} is the static magnetic force extracted from Eqn. (3.2). The static solution for Eq. (3.4) is calculated based on the geometric parameters given in Table 4.1. The static deflection of the cantilever beam varies with the separation of two magnets, as seen in Fig. 3.7. It is demonstrated conclusively that the static response has critical threshold separation distance d_{th} of $14.7mm$, that dividing the static profile into monostable ($d > d_{th}$) and bistable ($d \leq d_{th}$) regions. The monostable regime has a single stable branch for the static response, whereas the bistable regime has two stable branches (upper and lower). Due to the symmetry and the restriction from the lower electrode, only one branch of the horizontal beam's stable solution is presented in Fig. 3.7, where the maximum static deflection of the cantilever beam found to be at the bistable regime is 9.3 mm. Furthermore, the static deflections as a function with the separation distance between the two magnets are measured experimentally, and the results in Fig. 3.7 show a good agreement with the theoretical results.

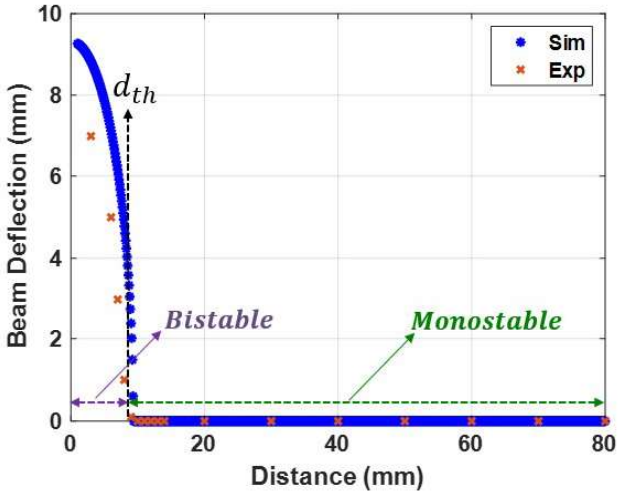

Figure 3.7. Experimental and theoretical static response of the beam as a function of the separation between the two magnets (d). The threshold distance (d_{th}) found to be 9 mm.

Dynamic Analysis

Natural Frequencies

Next, we will examine the effect of the magnetic force on the harvester's natural frequency. Toward this, the total deflection of the beam is taken to be a function of the static and dynamic deflections as ($y = y_s + y_u$), where, y_u is the dynamic deflection of the beam. By substituting this in Eq. (3.3), we end up with the following system of equations:

$$\begin{cases} m\ddot{y_u} + c\dot{y_u} + k_{eq}y_u + k_{eq}y_s - F_{magyus} + F_e = ma, & y_u(t) < g_i \\ \\ m\ddot{y_u} + c_i\dot{y_u} + k_{eq}y_u + k_{eq}y_s + k_i(y_u(t) + y_s - g_i) - F_{magyus} = ma, & y_u(t) \geqslant g_i \end{cases} . \tag{3.6}$$

$$\dot{q} = -\frac{q(t)}{\epsilon_0 RS}(\frac{T}{\epsilon_r} + d_0 - y_u(t) - y_s) + \frac{\sigma}{\epsilon_0 RS}(d_0 - y_u(t) - y_s)$$

Where, F_{magyus} is given by:

$$F_{magyus} = \frac{F_R(y_u + y_s)}{(d^2 + (y_u + y_s)^2)^{5/2}} \tag{3.7}$$

To eliminate the static effect and avoid the system's complexity while obtaining the numerical solution, the magnetic force, F_{magyus}, is expanded with Taylor's series around zero dynamic deflection $y_u = 0$ as follows:

$$\begin{aligned} F_{magyus} &= \frac{F_R y_s}{(d^2 + y_s^2)^{5/2}} + \alpha_1 y_u + \alpha_2 y_u^2 + +\alpha_3 y_u^3 + ... \\ &= F_{magys} + \alpha_1 y_u + F_{magyu} \end{aligned} \tag{3.8}$$

Where F_{magyu} is the dynamic portion of the expanded magnetic force omitting the linear term, and α_i represents the coefficient components of the magnetic force after Taylor series

expansion. The final form of the dynamic governing equation will be obtained by substituting Eq. (3.8) into Eq. (3.6) and then canceling the static terms using Eq. (3.4). This will result in the following:

$$\begin{cases} m\ddot{y_u} + c\dot{y_u} + (k_{eq} - \alpha_1)y_u - F_{magyu} + F_e = ma, & y_u(t) < g_i \\ m\ddot{y_u} + c_i\dot{y_u} + (k_{eq} - \alpha_1)y_u + k_i(y_u(t) + y_s - g_i) - F_{magyu} = ma, & y_u(t) \geqslant g_i \end{cases} . \tag{3.9}$$

$$\dot{q} = -\frac{q(t)}{\epsilon_0 RS}(\frac{T}{\epsilon_r} + d_0 - y_u(t) - y_s) + \frac{\sigma}{\epsilon_0 RS}(d_0 - y_u(t) - y_s)$$

According to Eqn. (3.9), the natural frequency of the nonlinear resonator under the effect of the magnetic force is calculated as:

$$f_n = \frac{1}{2\pi}\sqrt{\frac{k_{eq} - \alpha_1}{m}} \tag{3.10}$$

Where, α_1 is the linear coefficient of the dynamic magnetic force after the Taylor series expansion of Eq. (3.7) around $y = 0$, and given by:

$$\alpha_1 = \frac{F_R(d^2 - 4y_s^2)}{(d^2 + y_s^2)^{7/2}} \tag{3.11}$$

It is possible to determine the relationship between the natural frequency and the magnetic force by varying the distance between the two magnets and calculating the natural frequency value using Eq. (3.10). The natural frequency variation with the separation distance between the two magnets is shown in Fig. 3.8. The results show that bistable and monostable zones are separated by a threshold distance of 9 mm, which is consistent with the static results presented in Fig. 3.7. The system is in the bistable region at low separation distances, where the magnetic force exerts the most substantial effect. At this zone, the natural frequency reaches a higher frequency than the linear natural frequency and reaches a maximum value of 90 Hz. The natural frequency gradually decreases by increasing the distance between the two magnets until it reaches its minimum value at the threshold distance. Moreover, the system is tested experimentally at a 0.1 g excitation level, and the experimental variance of the natural frequencies with separation distance is obtained and presented as shown in Fig. 3.8. The experimental and simulated findings are in good agreement in the monostable range but not in perfect agreement in the transition and bistable ranges. The reason behind this difference could be the low accuracy of the SDOF model at high nonlinearities. Another reason could

be the experimental measurement errors. This slight difference between the experimental and simulated values of the natural frequencies would cause significant mismatch problems later when investigating the dynamic behavior of the harvester when we tried to validate our theoretical results. Therefore, this difference needs to be eliminated. Toward this, the experimental results for the variation of the natural frequencies are used to extract the experimental stiffness values shown in Fig. 3.9a. Then, a piece-wise curve fit function for the stiffness as a function of the separation distance between the two magnets is extracted and shown in Eq. (3.12). The piece-wise stiffness function is then used to calculate the natural frequencies, which greatly agree with experimental results as shown in Fig. 3.9b. Furthermore, the piece-wise stiffness function will be used in the further analysis of the dynamic behavior of the harvester.

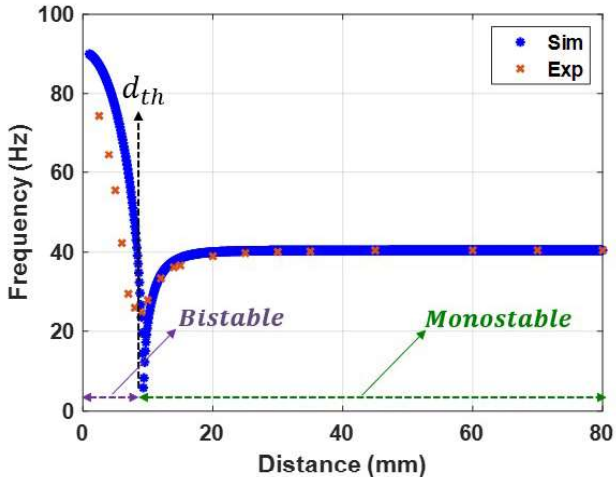

Figure 3.8. Variation in natural frequency with distance d between two magnets at 0.1g.

$$\begin{cases} k = 5956.75 - 4954.35d + 2004.2d^2 - 398d^3 + 37.16d^4 - 1.31d^5, & d < d_{th} \\ k = -937.71 + 224.567d - 16.7d^2 + 0.67d^3 - 0.01565d^4 + 0.000212d^5 - 1.5343e-6d^6 + 4.61e-9d^7, & d \geq d_{th} \cdot \end{cases} \tag{3.12}$$

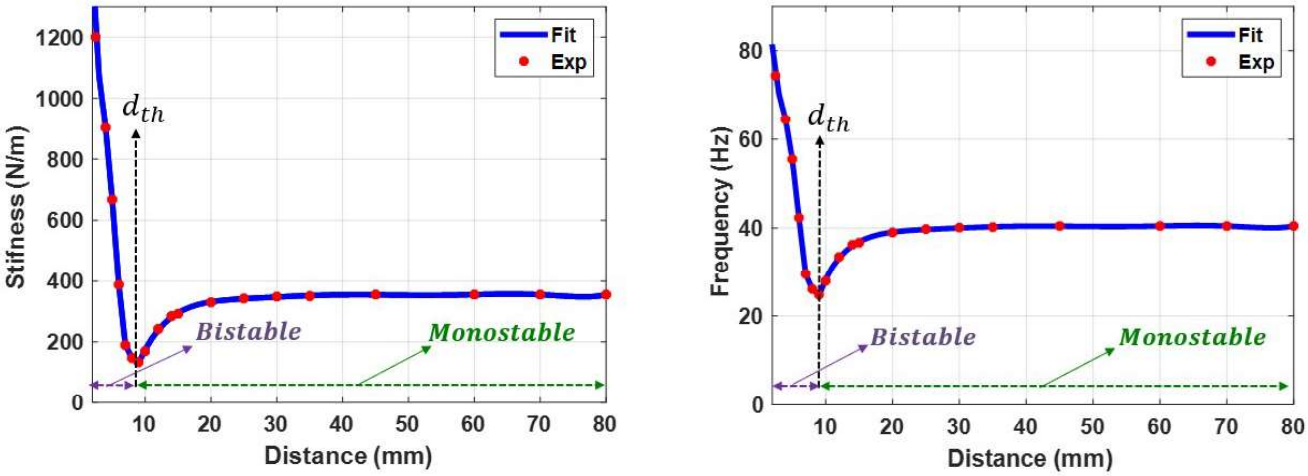

(a) **(b)**

Figure 3.9. (a) Variation in stiffness with distance d between two magnets (b) Variation in natural frequency with distance d between two magnets.

Linear and Conventional Harvester Analysis

Eliminating the influence of magnetic nonlinearity by setting F_{magyu} equal to zero allows for the investigation of the linear harvester behavior and the conventional Vibro-impact harvester. First, the linear harvester is investigated by exciting the system at a low excitation level of $0.1g$, which is insufficient to introduce the impact between the harvester's electrodes. The linear frequency voltage curve is shown in Fig. 3.10. The theoretical and experimental results are in high agreement. They show that the natural frequency of the harvester has a natural frequency of approximately $40.4Hz$. Second, the system is excited with higher excitation levels to investigate the behavior of the conventional Vibro-impact harvester. The experimental voltage frequency curves at different excitation levels are shown in Fig. 3.11a. The results show an increment in the output voltage with increasing the excitation level, reaching a maximum value of 2.2 V at an excitation level of 0.9 g. Furthermore, results in Fig. 3.11a depict a significant increase in the bandwidth due to the impact between the harvester's electrodes starting at 0.5 g excitation level and increasing significantly at higher excitation levels. In addition, the results in Fig. 3.11a show a softening behavior at low excitation levels (≤ 0.3 g) where the system's natural frequency is shifting to lower values to the left, while at higher excitation levels (≥ 0.3 g), the frequency tend to be shifted to a higher value to the right indicating hardening behavior. The combination of both behaviors is known as combined behavior, [63]. The experimental and its matches with simulated

results for each excitation level separately are shown in Fig. 3.11b-c, where the theoretical and experimental findings are in good agreement for all cases.

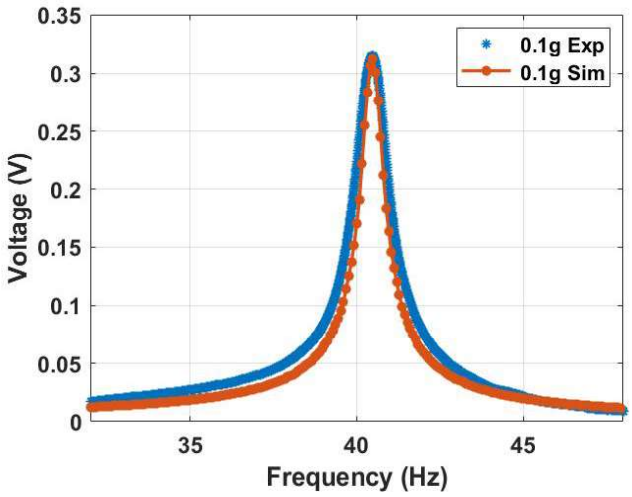

Figure 3.10. The linear experimental and theoretical frequency voltage curve without the influence of the magnetic force at at low excitation level of 0.1 g, $c = 0.03$, and $\sigma = 1.3\ \mu C/m^2$.

Nonlinear Analysis

In this section, we will investigate the dynamics of the energy harvester under the influence of the magnetic force at the monostable, bistable, and transition zones. The distance between the two magnets will be selected to achieve the required range, while the voltage responses will be analyzed at various excitation levels. First, we investigate the dynamics of the energy harvester in the monostable zone starting with a separation distance of $30mm$. The

experimental voltage frequency curves with the corresponding simulated results for different excitation levels are shown in Fig. 3.12 and reflect high agreements. Comparing the results at a $30mm$ (Fig. 3.12) with the previous results under no magnetic effect (Fig. 3.11), we notice that the results are quite close to each other. This is because the two magnets are far from each other at this distance, and the magnetic force is feeble, so its effect is almost neglected. It should also be noted that greater excitation levels result in higher output voltage and bandwidth. Moreover, the combined behavior is shown in the results with softening behavior is dominant at low excitation levels. In contrast, the hardening behavior is dominant at higher excitation levels.

Next, we set the distance between the two magnets to $20mm$ to investigate the dynamic behavior in the monostable range, but at a stronger magnetic force influence. The results in Fig. 3.13 show the frequency voltage curves extracted experimentally and matched with the simulations from the theoretical model at a good agreement. According to the results shown in Fig. 3.13, several things can be noticed. First, we can notice that the natural frequency is shifted to the left to reach a lower value of 38.7 Hz compared to the conventional and 30 mm frequencies. This shift is due to the effect of the higher magnetic nonlinearity at this distance compared to the previous cases. This led to a lower beam's natural frequency according to the results presented in Fig. 3.9b. Second, larger bandwidth is achieved by increasing the

excitation level, where the impact between the harvester becomes more significant, and a wider range of frequencies compared to the low excitation levels. Also, in the $20mm$ case, the bandwidth is slightly larger than the conventional and 30 mm bandwidth. This slight difference is because even though the magnetic force is stronger than in the previous cases, it is still considered feeble. Third, the output voltage increases with the excitation level, which also can be related to the higher impact between the harvester electrodes at higher excitations. However, the output voltage at this distance is less than the conventional and 30 mm output voltage.

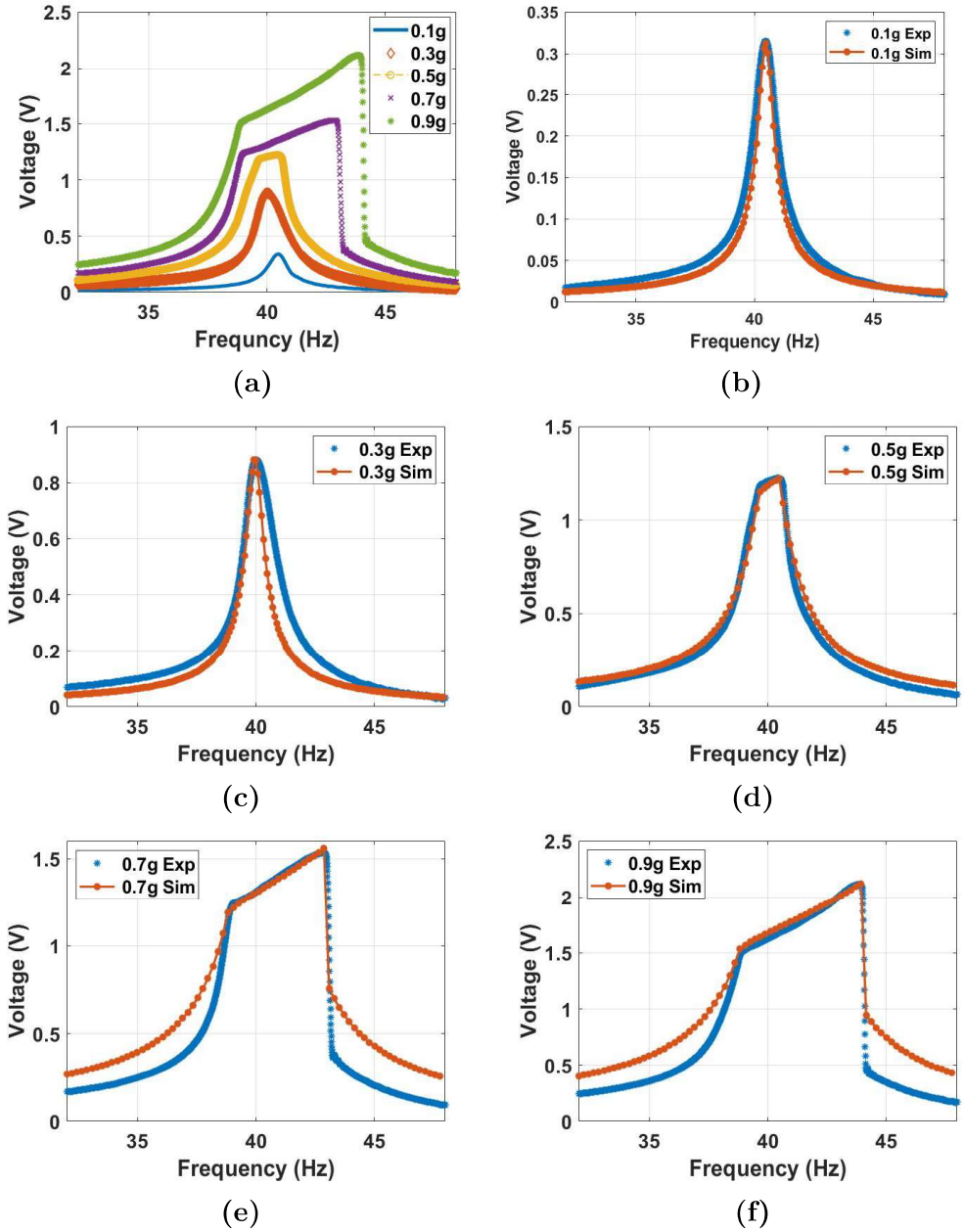

Figure 3.11. The frequency voltage curve of the beam at different excitation levels without magnetic force effect: (a) experiment results (b) $0.1g$, $c = 0.03$, and $\sigma = 1.35\ \mu C/m^2$ (C) $0.3g$, $c = 0.0335$, and $\sigma = 1.4\ \mu C/m^2$ (d) $0.5g$, $c = 0.05$, and $\sigma = 2.8\ \mu C/m^2$ (e) $0.7g$, $c = 0.03$, and $\sigma = 4.2\ \mu C/m^2$ (f) $0.9g$, $c = 0.03$, and $\sigma = 5.2\ \mu C/m^2$.

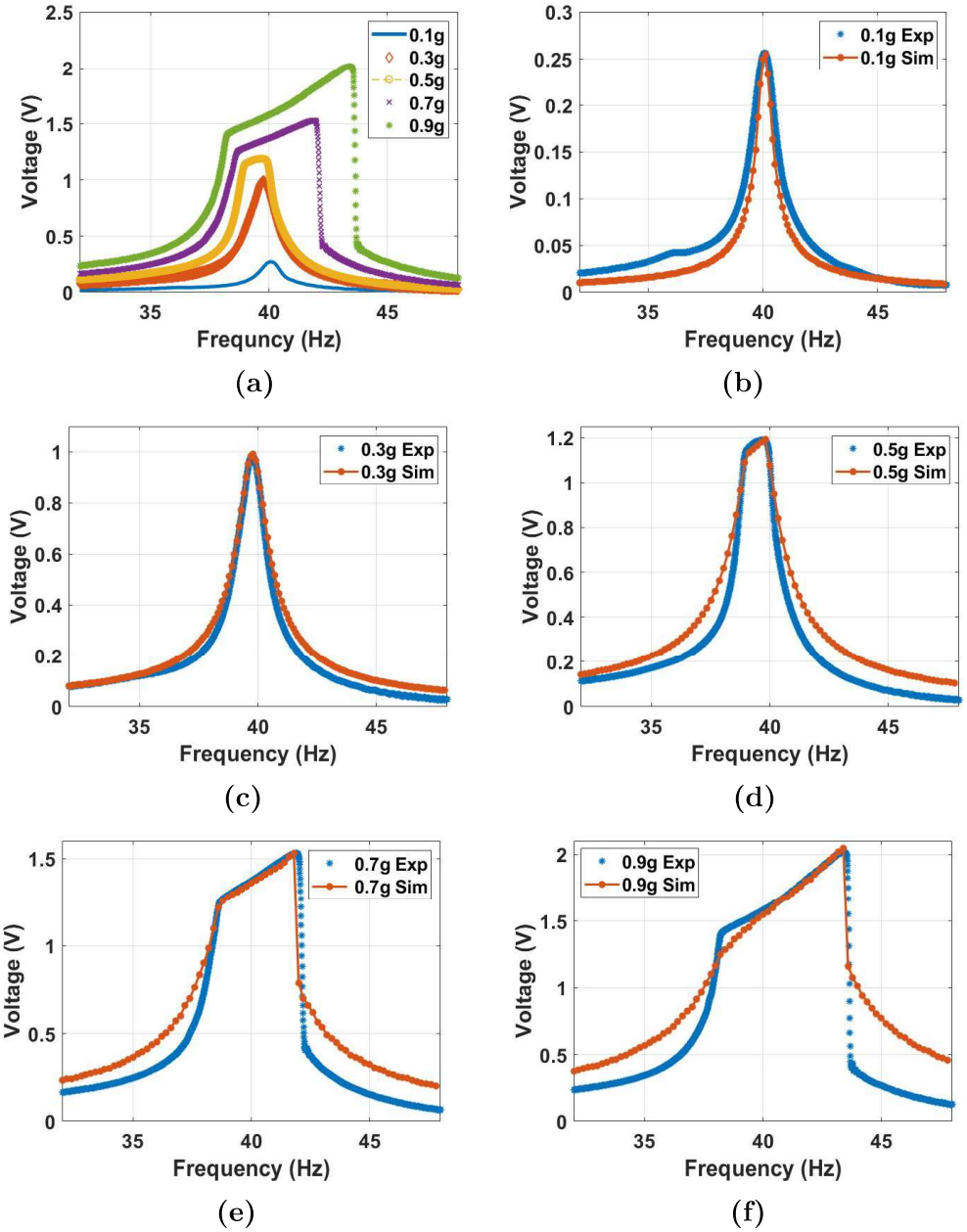

Figure 3.12. The voltage frequency response curve of the monostable at $d = 30mm$ at different excitation levels: (a) experiment results (b) $0.1g$, $c = 0.02$, and $\sigma = 1.06\ \mu C/m^2$ (C) $0.3g$, $c = 0.04$, and $\sigma = 2.7\ \mu C/m^2$ (d) $0.5g$, $c = 0.05$, and $\sigma = 3.9\ \mu C/m^2$ (e) $0.7g$, $c = 0.009$, and $\sigma = 2.96\ \mu C/m^2$ (f) $0.9g$, $c = 0.001$, and $\sigma = 2.9\ \mu C/m^2$.

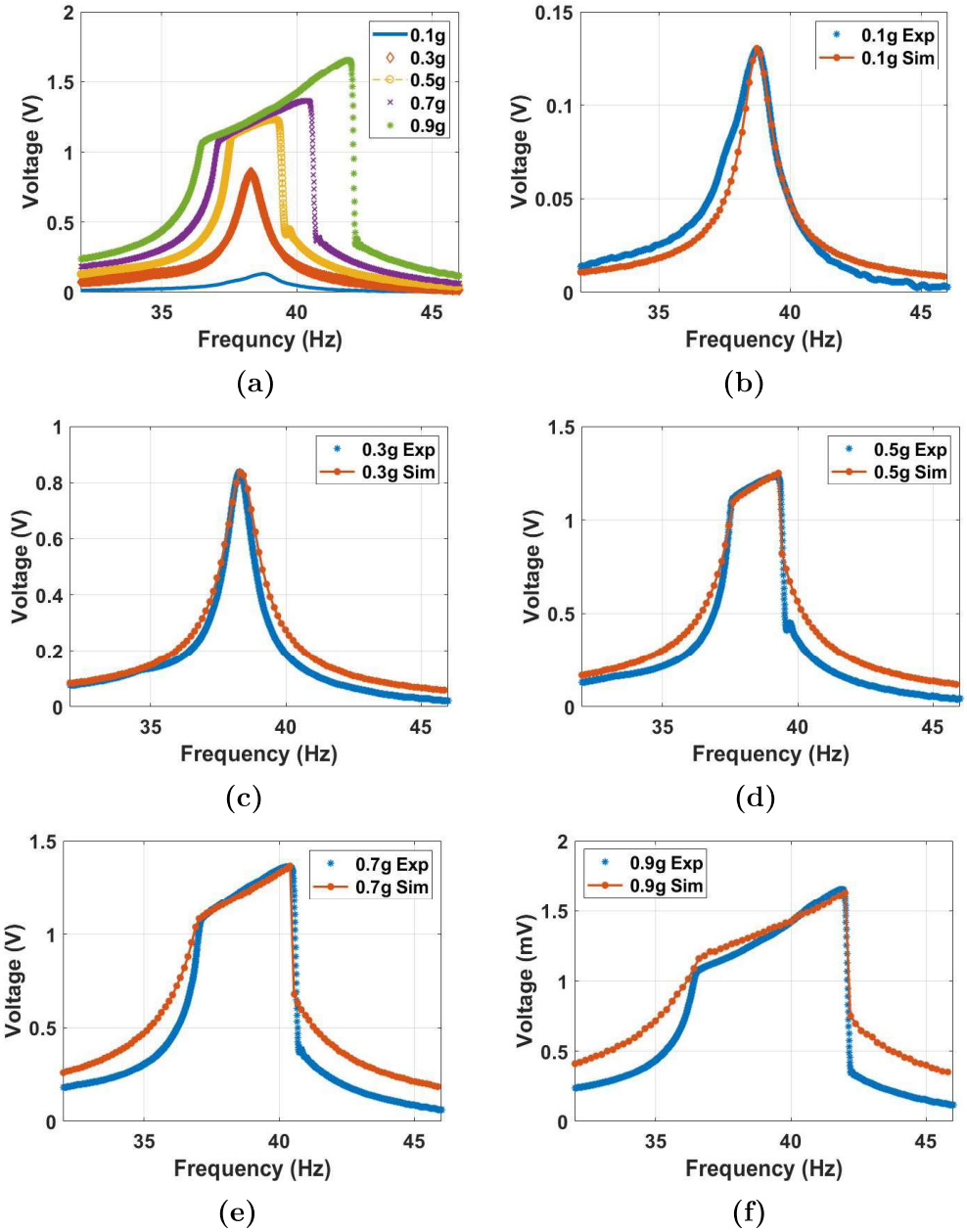

Figure 3.13. The voltage frequency response curve of the monostable at $d = 20mm$ at different excitation levels: (a) experiment results (b) $0.1g$, $c = 0.035$, and $\sigma = 0.91\ \mu C/m^2$ (C) $0.3g$, $c = 0.04$, and $\sigma = 2.2\ \mu C/m^2$ (d) $0.5g$, $c = 0.035$, and $\sigma = 2.68\ \mu C/m^2$ (e) $0.7g$, $c = 0.02$, and $\sigma = 2.93\ \mu C/m^2$ (f) $0.9g$, $c = 0.01$, and $\sigma = 3.5\ \mu C/m^2$.

By lowering the separation distance between the two magnets more, particularly to 12mm, the system will enter the transition range from the monostable side. The frequency voltage curves for 12 mm distance at different excitations from both experimental and simulations are shown in Fig. 3.14 with a good agreement. The results show a shift in the natural frequency to a lower value of 33.5 Hz, indicating softening behavior. Moreover, higher bandwidth is achieved even at lower excitations, where the impact between the harvester's layers is started at 0.3 g compared to 0.5 g in all the previous cases and increases significantly at higher excitation levels. A maximum bandwidth of 7.5 Hz is achieved at 0.9 g compared to 5.0 Hz in the previous cases at the same excitation level, which is equivalent to 50 % increment. This increment in the bandwidth at low excitation is due to the effect of the magnetic force, which starts to be stronger and more significant at a lower distance. In addition, the output voltage increases significantly by 60 % with the increasing excitation level to reach a maximum value of 3.2 V compared to a maximum output voltage of 2.0 from the conventional harvester at the same excitation level. Furthermore, a hardening behavior starts to show up by increasing the excitation level, which indicates the dominance of the positive cubic nonlinearity from the magnetic force, shifting the whole behavior to the right.

Lowering the separation distance to 10.0 mm will result in lowering the natural frequency to a lower value, and the softening behavior becomes more significant. At the same time, a

wider bandwidth is achieved compared to the previous cases, as shown in Fig. 3.15. However, the voltage amplitude is showing a reduction compared to the 12 mm case, which could be due to the effect of the static magnetic force that reduces the gap between the two electrodes and results in broader bandwidth, and at the same time, restricts the beam from oscillating freely.

By decreasing the distance more to reach the threshold at d_{th}, the bandwidth increases even more than all the previous cases at the same excitation levels, as shown in Fig. 3.16. However, this increment in the bandwidth is at the cost of the voltage output since it is dropped to a maximum value of 2.4 V at 0.9 g. The drop in the voltage out is expected because the natural frequency reaches the lowest value of 24.8 Hz, which matches the results in Fig. 3.9b. This drop in the natural frequency to a lower value indicates softening behavior compared to the linear harvester. It is due to the predominance of quadratic nonlinearity at the threshold distance.

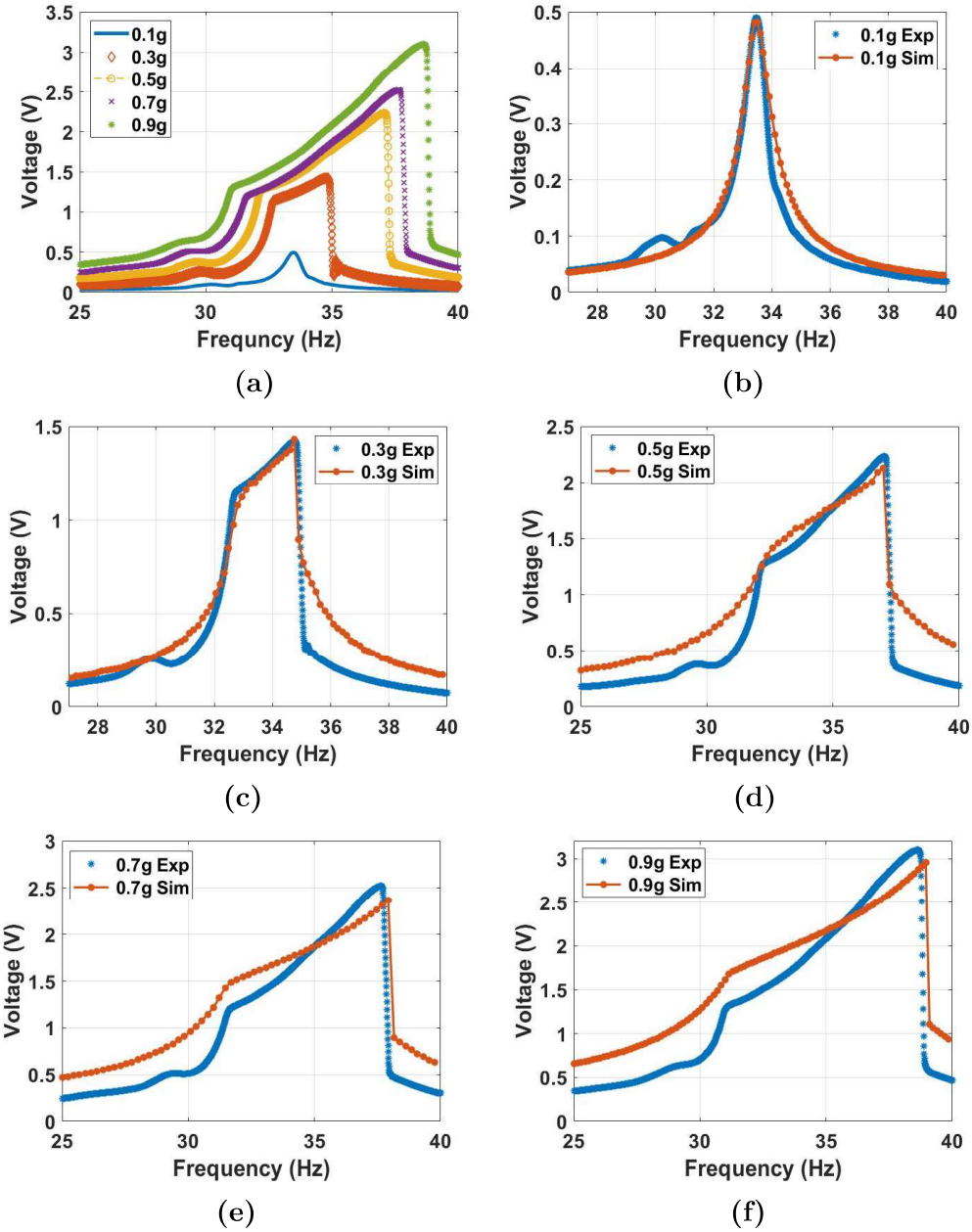

Figure 3.14. The voltage frequency response curve of the monostable at $d = 12mm$ at different excitation levels: (a) experiment results (b) $0.1g$, $c = 0.03$, and $\sigma = 2.5\ \mu C/m^2$ (C) $0.3g$, $c = 0.001$, and $\sigma = 2.6\ \mu C/m^2$ (d) $0.5g$, $c = 0.003$, and $\sigma = 4.7\ \mu C/m^2$ (e) $0.7g$, $c = 0.02$, and $\sigma = 6.4\ \mu C/m^2$ (f) $0.9g$, $c = 0.04$, and $\sigma = 7.4\ \mu C/m^2$.

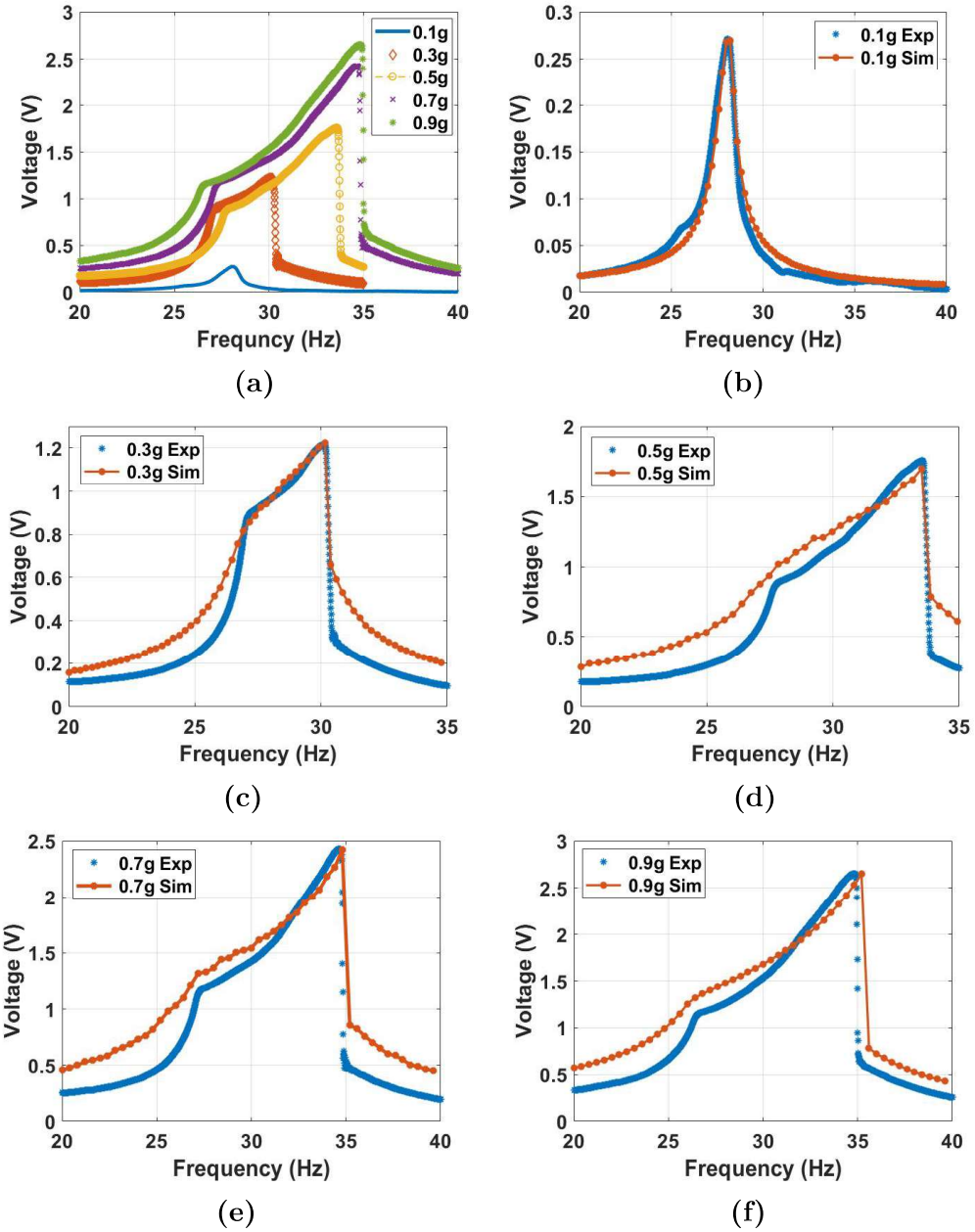

Figure 3.15. The voltage frequency response curve of the monostable at $d = 10mm$ at different excitation levels: (a) experiment results (b) $0.1g$, $c = 0.03$, and $\sigma = 1.19\ \mu C/m^2$ (C) $0.3g$, $c = 0.001$, and $\sigma = 2.45\ \mu C/m^2$ (d) $0.5g$, $c = 0.0035$, and $\sigma = 4.1\ \mu C/m^2$ (e) $0.7g$, $c = 0.006$, and $\sigma = 5.2\ \mu C/m^2$ (f) $0.9g$, $c = 0.03$, and $\sigma = 5.65\ \mu C/m^2$.

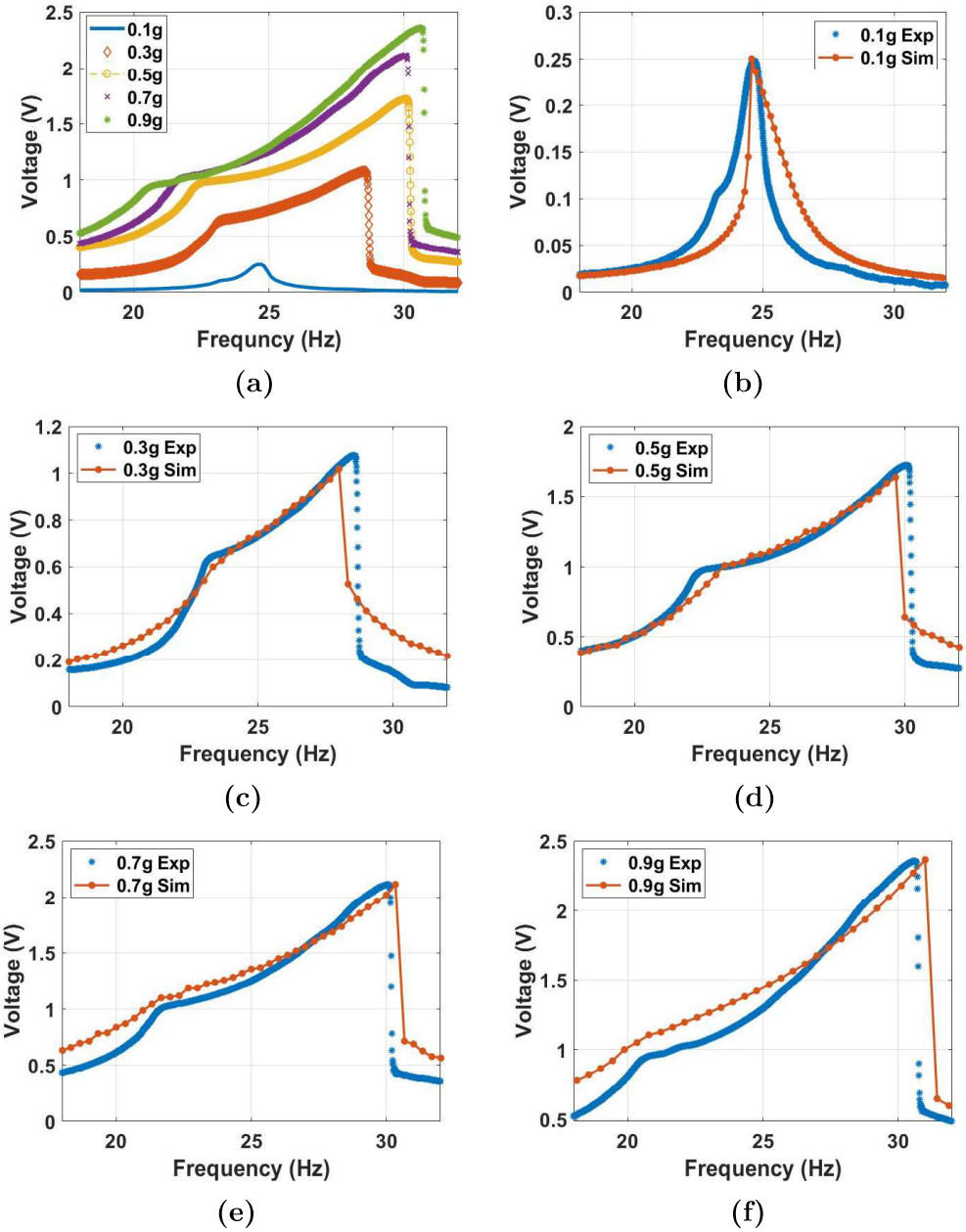

Figure 3.16. The voltage frequency response curve of the threshold at $d = 9mm$ at different excitation levels: (a) experiment results (b) $0.1g$, $c = 0.03$, and $\sigma = 1.01\ \mu C/m^2$ (C) $0.3g$, $c = 0.001$, and $\sigma = 2.4\ \mu C/m^2$ (d) $0.5g$, $c = 0.0065$, and $\sigma = 4\ \mu C/m^2$ (e) $0.7g$, $c = 0.008$, and $\sigma = 4.4\ \mu C/m^2$ (f) $0.9g$, $c = 0.025$, and $\sigma = 4.6\ \mu C/m^2$.

In order to further investigate the dynamic behavior of the harvesting system at the threshold distance, the harvester's time response, phase portrait, and time-voltage/velocity are extracted at specific frequencies to reflect the response before-impact, during-impact, and after-impact zones, as shown in Fig. 3.17. Before the impact, at 19 Hz, the maximum harvester oscillation is around 0.8 mm, which is less than the gap between the harvester's electrodes (1.0 mm) as shown Fig. 3.17a. The corresponding phase portrait and voltage output are shown in Fig. 3.17b, and c, respectively. The phase portrait reflects stable oscillation without any sudden change in the velocity, which is an indication of no impact at this frequency. The voltage output in Fig. 3.17c, is small since it is only due to the effect of the capacitance. By increasing the excitation frequency to 24.8 Hz, the oscillations reach the gap distance, Fig. 3.17d, and the during-impact zone occurs between the harvester electrodes, as shown by the sudden change in the velocity and the restriction of the displacement in the phase portrait, Fig. 3.17e. This impact will activate the contact electrification process, and higher voltage output can be generated, as shown in Fig. 3.17f. When the excitation frequency exceeds 31.06 Hz, the system enters the after-impact zone, which is similar in behavior to the before-impact zone, as shown in Figures. 3.17g-i.

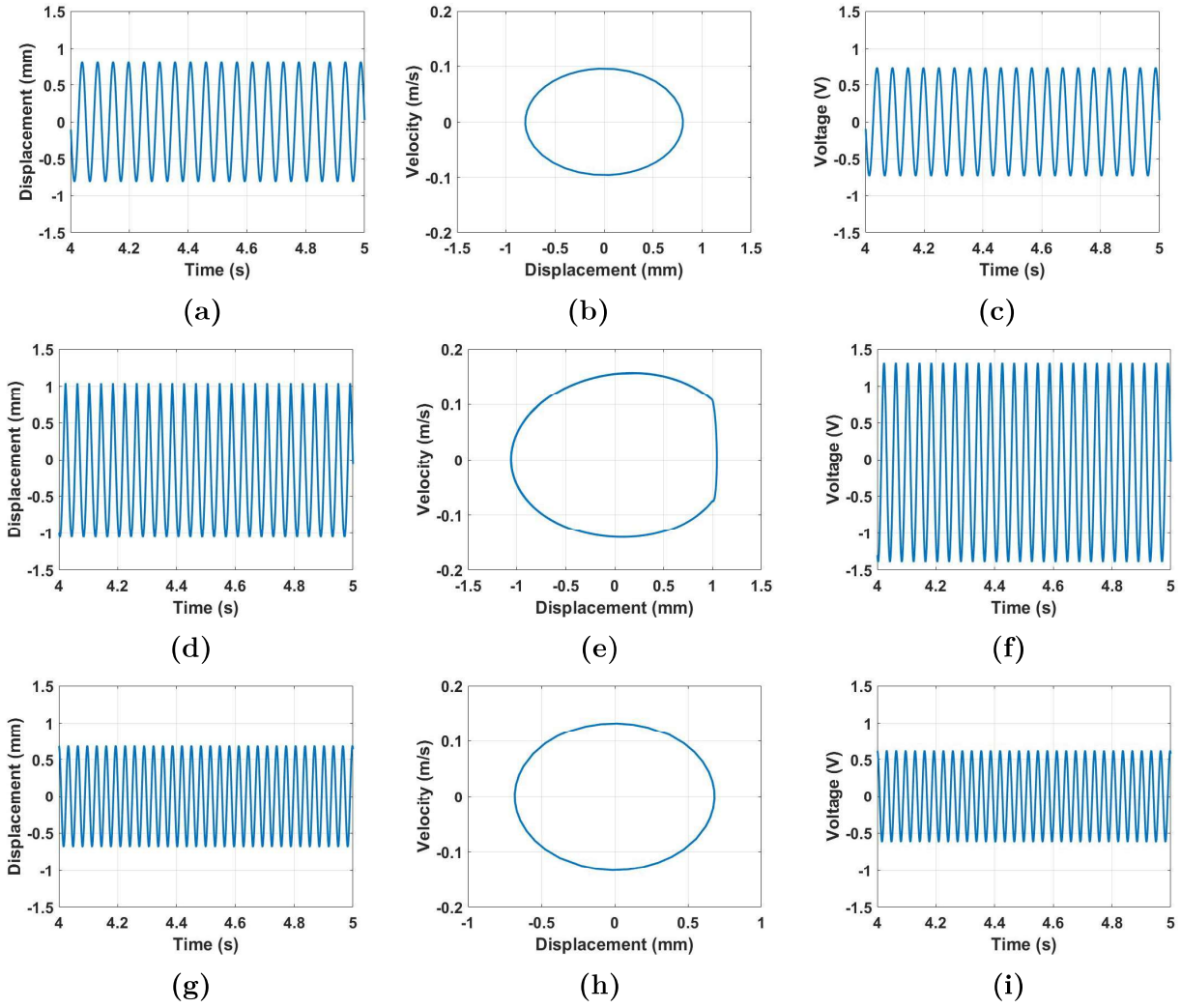

Figure 3.17. Response and output voltage at a variety of frequencies when the distance d is set at $9mm$.

At a distance below the threshold value, the magnetic nonlinearity becomes very strong. Experimentally, and under the base excitations, it deflects the beam to the degree where the attractive magnetic force between the two magnets becomes significant and causes the

tip magnet to stick with the fixed one, hence leading to a failure in the system. Therefore, since we validated our theoretical model experimentally, the dynamic behavior of the energy harvester in the bistable range will be explored through the theoretical model only. Toward this, the distance between the two magnets is lowered to 8 mm, 5 mm, and 4 mm, as shown in Fig. 3.18. At 8 mm, Fig. 3.18a, the system still shows an impact behavior close to the range of frequencies at the threshold. Also, the generated voltage dropped significantly to 2.24 V. Furthermore, a hardening behavior is shown by increasing the excitation level. Lowering the separation distance to the lower values 5 mm, and 4 mm will increase the natural frequencies to reach higher values of $55.3Hz$ and $64.25Hz$, respectively, indicating a hardening behavior. This significant increment in the natural frequency in the system is due to the strong magnetic nonlinearity induced at lower separation distances. However, increasing the excitation level will force the system to have softening behaviors, where the quadratic nonlinearity becomes dominant, shown in Fig. 3.18b, and c. Furthermore, the impact bandwidth becomes smaller at 5 mm and 4 mm, while the output voltage reaches the lowest values compared to all the previous cases. Even though the system reaches higher frequencies at lower distances, the output voltage is minimized, possibly due to the high magnetic force that forces the beam's tip magnet to get stuck at one of the potential wells and restrict its oscillations. Therefore, it is anticipated that the deflections will be smaller than the distance between the triboelectric harvester's electrodes.

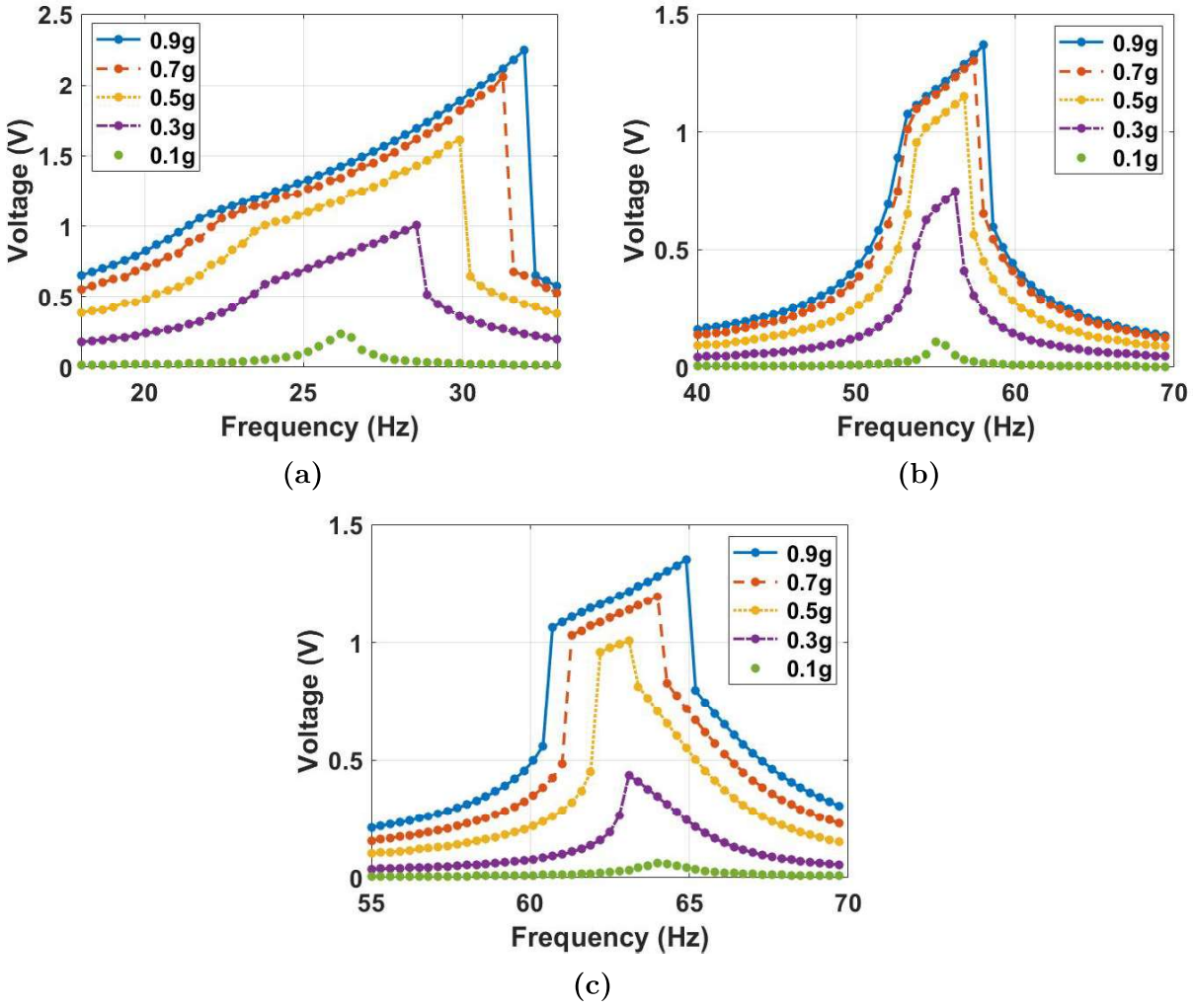

Figure 3.18. The voltage frequency response curve of the bistable at: (a) $d = 8\ mm$ and $\sigma = 1\ \mu C/m^2$ (b) $d = 5\ mm$ and $\sigma = 1\ \mu C/m^2$ (c) $d = 4\ mm$ and $\sigma = 1\ \mu C/m^2$.

Next, to have an indication of the optimal range for the proposed harvester, we calculated the impact bandwidth and voltage output of the harvester at a selected excitation level of 0.9 g for all the previous cases as a function of the separation distance between the two magnets, as shown in Fig. 3.19. It is clear that the bandwidth is maximized in a range just

before and after the threshold distance (9.0 mm). This range is known as the transition regime. It was found that an increment in the bandwidth of around 110.41 % is achieved at the transition region of the nonlinear harvester compared to the conventional harvester presented in Fig. 3.11f, at an excitation level of 0.9 g. Furthermore, the output voltage is maximized around the threshold distance in a similar way for the bandwidth, as shown in Fig. 3.19b. Therefore, the transition region is considered the optimal region for the harvester to operate since the bandwidth and voltage output will be maximized, allowing more energy to be harvested from the ambient excitations.

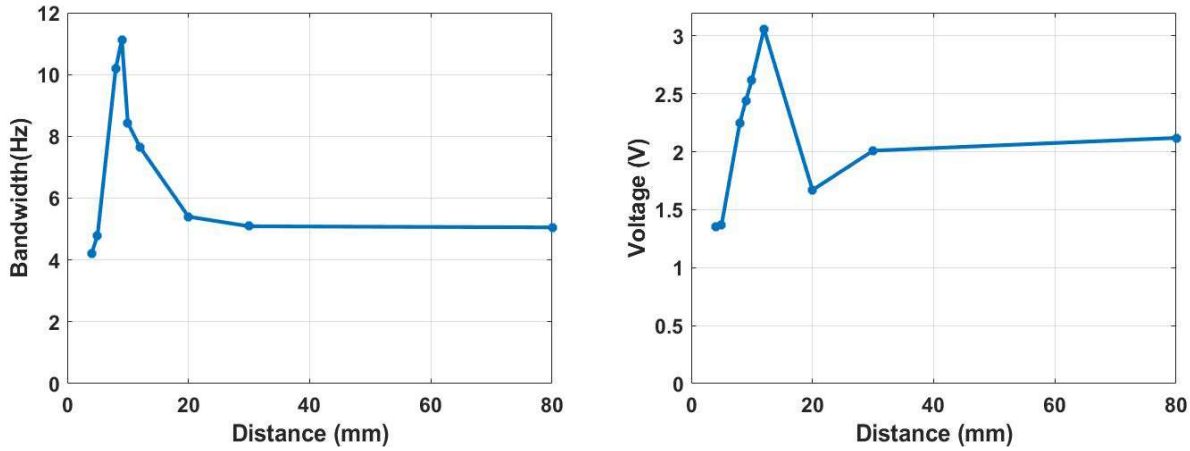

(a) (b)

Figure 3.19. (a) Comparison between bandwidth and magnet separation distance at 0.9g (b) Voltage output vs d at 0.9g.

Parametric Analysis

It is essential to explore the effect that external resistance has on harvester performance since it directly influences the amount of power produced. To do this, we fixed the distance between the two magnets at $d = 9\ mm$ and varied the resistance from 10 $M\Omega$ to 30 $M\Omega$ at 0.9 g excitation level, as seen in Fig. 3.20a. As a result, a higher voltage signal is generated at higher external resistance, with a maximum of 4.8 V at a resistance of 30 $M\Omega$. Moreover, the output power was calculated at different resistance values, as shown in Fig. 3.20b. As a result, it is demonstrated that the power increases by increasing the resistance until it reaches its maximum value of 15 μW at a resistance of 30 $M\Omega$. However, a further increment in the external resistance will continue the increment in the output power until it reaches the maximum possible power where the external resistance matches the internal resistance of the harvester. Beyond this value, the output power will start to drop. Therefore, it is worth mentioning that the internal resistance needs to be extracted for practical applications to enhance the triboelectric energy harvester's performance and maximize the power output.

To further investigate the effect of the parameters on the harvester performance, we investigate the impact of the gap distance between the harvester's electrodes. Toward this, the system is excited at 0.9 g excitation level for various values of the gap distance as shown in Fig. 3.21a. It depicts that wider bandwidth is possible at lower gaps., while greater amplitudes can be

achieved at higher gaps but at the expense of bandwidths. At lower gaps, more contact will occur at a wider range of frequencies, resulting in a wider bandwidth. Conversely, higher gaps lead to less contact at a narrower frequency range resulting in a limited bandwidth. Moreover, the surface charge density is an additional important component that substantially impacts the magnitude of the voltage generated. The voltage amplitude fluctuation under various surface charge density values is depicted in Fig. 3.21b at an excitation level of 0.9 g, and magnets spacing of 9 mm, while all other parameters are held constant. The results indicate that as the charge density increases, the voltage amplitudes grow significantly. It is important to note that the surface charge density is a function of the surface area of contact between the triboelectric layers. Designing such layers with micro-surface patterns is one of the primary characteristics that could increase this charge density and result in higher generated voltage.

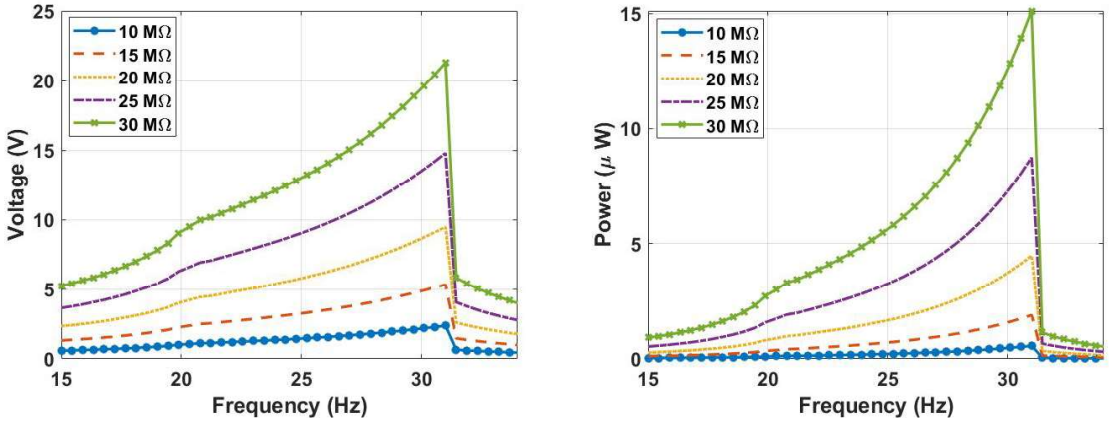

(a) (b)

Figure 3.20. The frequency voltage and power curves at 0.9 g excitation level, 9 mm separation distance at various resistance (R).

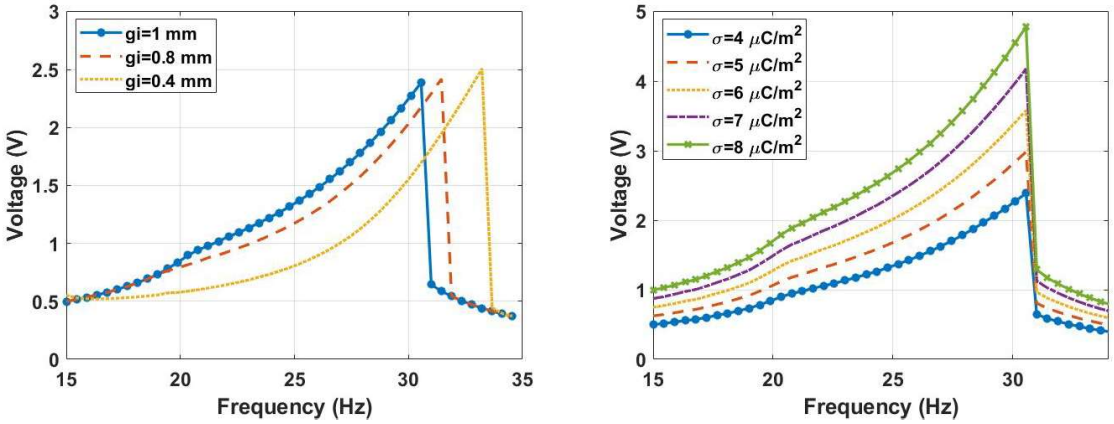

(a) (b)

Figure 3.21. The frequency voltage curve at 9 mm of separation distance (a) varying gap distances g_i (b) various surface charge densities σ.

At an excitation level of 0.9 g, the investigation into the impact of the gap separation between the harvester's layers is examined, as shown in Fig. 3.20c. When gap lengths

are decreased, wider voltage bandwidths are possible to achieve. Higher separation gaps, exceeding 1 millimeter, allowing for greater amplitudes to be achieved, but at the expense of narrower bandwidths. This is because a narrower gap suggests that the contact will take place over a larger range of frequencies, which ultimately results in a wider bandwidth. On the other side, larger gaps lead to fewer contacts, and a narrower frequency range results in a narrower bandwidth. Both of these effects are due to the fact that the gap size increases.

Chapter Four

Theoretical Investigation of Vibro-Impact Triboelectric Energy Harvester with Magnetically Adjustable Frequency for a Wider Bandwidth

In this chapter, modeling of a triboelectric vibration energy harvester under magnetic effect will discussed.. This work is similar to [63], but under the contribution of the triboelectric transduction mechanism. The harvester consists of a polymer cantilever beam attached to a tip magnet aligned with another fixed magnet at the same polarity to induce a nonlinear magnetic repulsive force. Under base excitation, the system vibrates and leads to a contact-separation motion between the two electrodes, generating a wide-band AC electrical signal.

Device Configuration and Operation

The vibro-impact energy harvester system that has been proposed is made up of a polymer cantilever beam with a tip magnet that is positioned to face another fixed magnet with the same polarity in order to produce a repulsive magnetic force. This configuration is depicted in Figure 4.1. By controlling the distance d between the two magnets, the repulsive magnetic force will force the beam to oscillate in either mono-or bistable regimes. The system utilizes a triboelectric mechanism for power generation, where the lower surface of the beam's tip magnet is made of Aluminum and acts as the upper electrode of the triboelectric energy harvester. The upper electrode is placed at a gap distance from Polydimethylsiloxane (PDMS) insulator bonded to another lower electrode attached to a base that holds the whole system and is subjected to harmonic excitation. The triboelectric generator comprises two layers with opposing electron loss and gain tendencies. Charges are generated through contact electrification, and electrostatic induction [59]. When the base excitation is high enough, the beam vibrates, and the displacement of the tip mass will exceed the gap causing a periodic impact between triboelectric generator's electrodes. This contact separation mechanism results in an alternative electrical signal being generated.

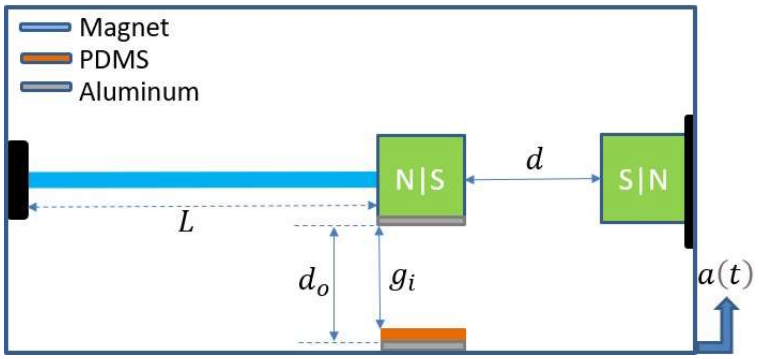

Figure 4.1. Schematic of the proposed bi-stable triboelectric energy harvester under base excitation.

Results and Discussion

In this section, the system is numerically solved and experimentally validated to facilitate further analysis, identify the crucial elements that will lead to a more effective energy harvester, and examine the potential for energy scavenging in the proposed harvester.

Table 4.1. Physical and geometrical parameters to be used in the model.

Parameters	**Symbol**	**Value**
Beam (*length* ×*width* × *thickness*)	$L \times b \times h$	$(40 \times 10 \times 1)$ mm
Beam Young's modulus	E	2.344 Gpa
Beam Density	ρ	1220 kg/m^3
Mass of the beam	M	5.5 gm
Beam Damping coefficient	c	0.04 N.s/m
Impact Damping coefficient	c_i	130 c N.s/m
Impact stiffness	k_i	130 k_{eq} N/M
Gap between top aluminum layer and PDMS	g_i	0.001 m
PDMS layer thickness	T	400×10^{-6} m
Resistance	R	10 MΩ
Magnets side length	L_m	8.0 mm
Magnetic moment	$q_1 = q_2$	0.5 A$^2/m$
PDMS (*length* ×*width* × *thickness*)	$L_p \times b_p \times h_p$	$(20 \times 20 \times 1)$ mm
PDMS vacuum permittivity	ϵ_0	8.854×10^{-12}

Linear and Conventional Harvester Analysis

Eliminating the influence of magnetic nonlinearity by setting F_{magyu} equal to zero allows for the investigation of the linear harvester behavior and the conventional Vibro-impact harvester. First, the linear harvester is investigated by exciting the system at a low excitation level of 0.1 g, which is insufficient to introduce the impact between the harvester's electrodes. The system is excited with higher excitation levels to investigate the behavior of the conventional Vibro-impact harvester as shown in Fig. 4.2. They show that the natural frequency of the harvester has a natural frequency of approximately 35 Hz. The results show an increment in the output voltage with increasing the excitation level, reaching a maximum value of 2.3 V at an excitation level of 0.9 g. Furthermore, results in Fig. 4.2a depict a significant increase

in the bandwidth due to the impact between the harvester's electrodes starting at 0.3 g excitation level and increasing significantly at higher excitation levels.

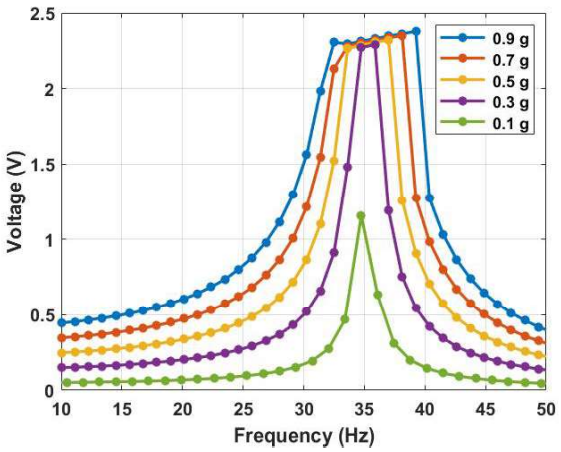

Figure 4.2. The resonance frequency of the Vibro-impact harvester without magnetic effect.

Nonlinear Analysis

In this section, we will investigate the dynamics of the energy harvester under the influence of the magnetic force at the monostable, bistable, and transition zones. The distance between the two magnets will be selected to achieve the required range, while the voltage responses will be analyzed at various excitation levels. First, we investigate the dynamics of the energy harvester in the monostable zone starting with a separation distance of $40mm$ and $25mm$. Comparing the results at a $40mm$ (Fig. 4.3a) with the previous results under no magnetic

effect (Fig. 4.2), we notice that the results are quite close to each other. This is because the two magnets are far from each other at this distance, and the magnetic force is feeble, so its effect is almost neglected. The magnetic nonlinearity increased by reducing the distance to 25 mm, resulting in a lower beam's natural frequency, higher amplitude achieved, and greater bandwidth at the same excitation levels as shown in (Fig. 4.3b). It should also be noted that greater excitation levels result in higher output voltage and bandwidth.

By lowering the separation distance between the two magnets more, particularly to 17 mm and 16 mm, the system will enter the transition range from the monostable side. The frequency voltage curves for 17 mm and 16 mm distances at different excitations simulations is shown in Fig. 4.4. The results show a shift in the natural frequency to a lower value of 25.1 Hz and 20.2 Hz respectively, indicating softening behavior. Moreover, higher bandwidth is achieved even at lower excitations, where the impact between the harvester's layers is started at 0.3 g, and increases significantly at higher excitation levels.

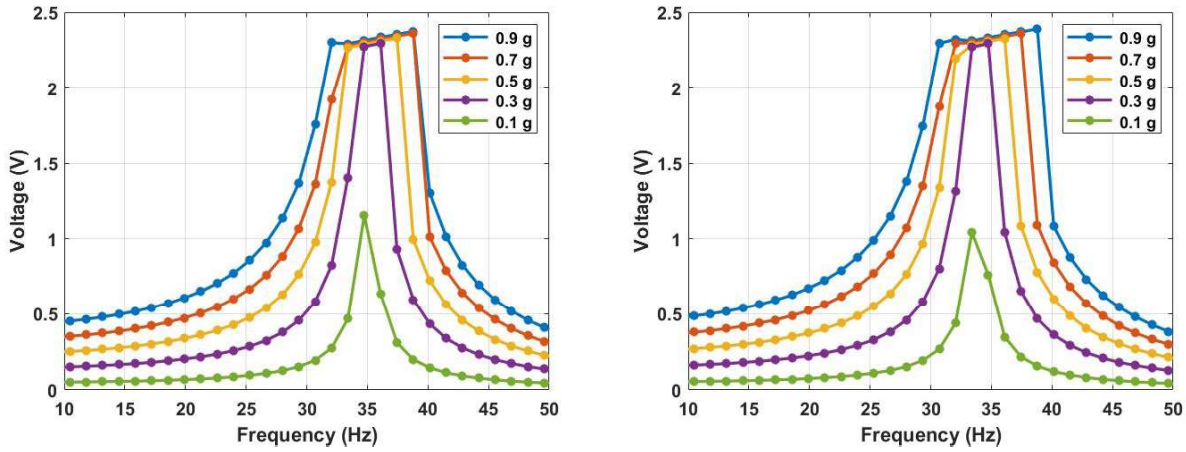

(a) (b)

Figure 4.3. The frequency voltage curve of the beam at different excitation levels: (a) 40 *mm* separation distance, (b) 25 *mm* separation distance.

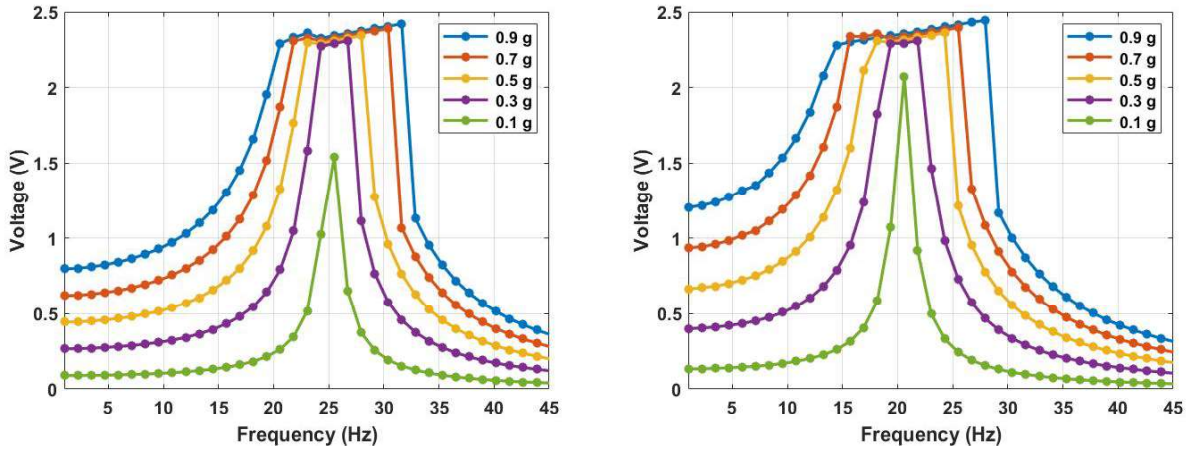

(a) (b)

Figure 4.4. The frequency voltage curve of the beam at different excitation levels: (a) 17 *mm* separation distance, (b) 16 *mm* separation distance.

Second, the frequency voltage curve is extracted for the transition region from the bistable side, specifically at 14.0 *mm* and 14.3 *mm* separation distances, as shown in Figure 4.5. The results show a shift in the natural frequency to a lower value of 18 Hz and 23.5 Hz respectively, indicating softening behavior. Higher bandwidth is shown at 14.3 *mm* compared to 14.0 *mm* indicating that the bandwidth is broadened at the transition region.

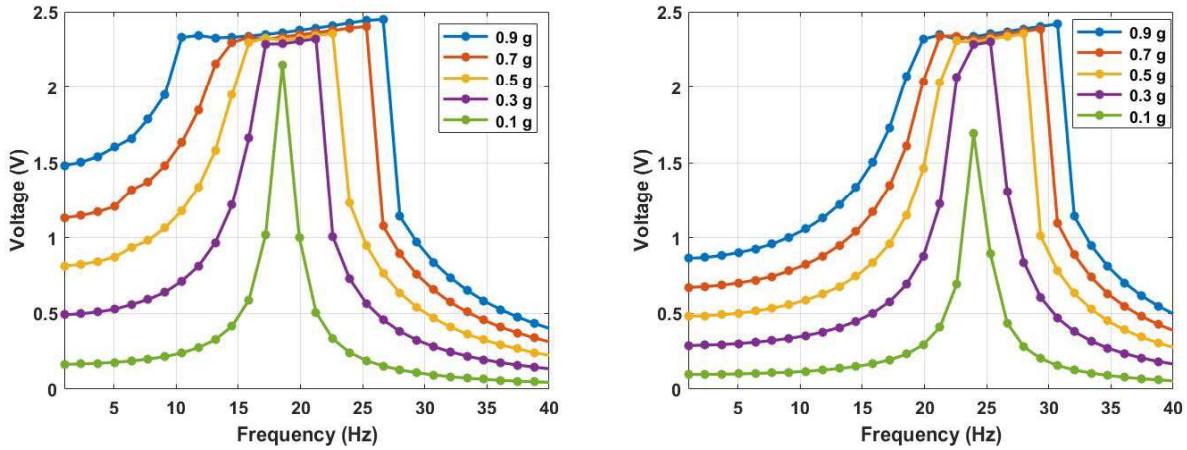

Figure 4.5. The frequency voltage curve of the beam at different excitation levels: (a) 14.3 *mm* separation distance, (b) 14 *mm* separation distance.

Decreasing the separation distance to reach $d = 15.5$ *mm* results in a softening behavior where the natural frequency is lower than the previous cases, as shown in Figure 4.6. Compared to previous cases, the highest bandwidth was achieved at this separation distance. Maximum bandwidth is achieved at 0.9 g which is higher compared the previous cases at the same excitation level. This increment in the bandwidth at low excitation is due to the effect

of the magnetic force, which starts to be stronger and more significant at a lower distance. In addition, the output voltage increases significantly with the increasing excitation level to reach a maximum value of 2.5 V compared to a maximum output voltage of 2.3 from the conventional harvester at the same excitation level.

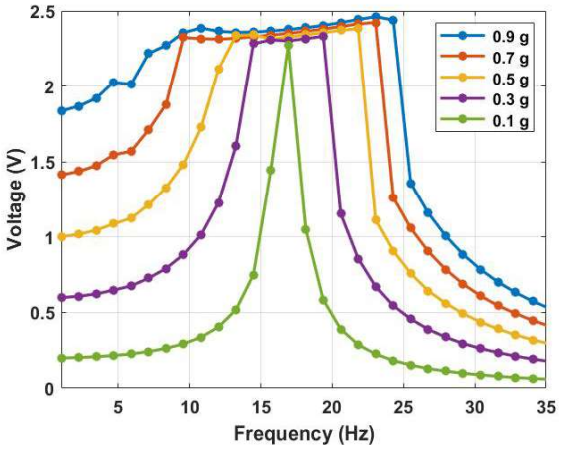

Figure 4.6. The voltage response curve of the beam at different excitation levels: 15.5 mm separation distance, $g_i = 1mm$.

By measuring the bandwidth at the 0.9 g excitation level from all the previously discussed separation distances, we find that the transition region is the optimal region for expanding the operating bandwidth of the harvester, as shown in Figure 4.7.

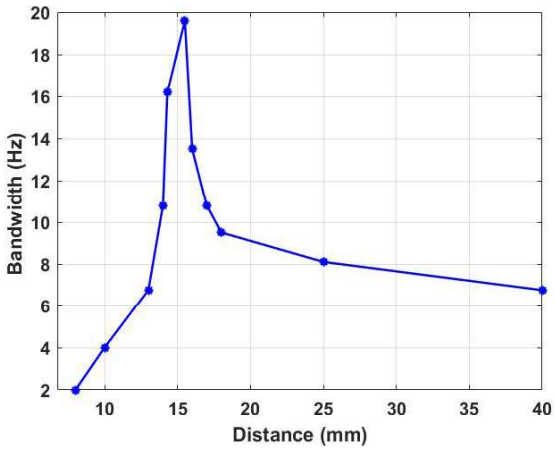

Figure 4.7. Comparison between bandwidth and separation distance between magnets at 0.9 g and $g_i = 1\ mm$.

To study further the important aspects influencing the efficiency of the proposed harvester, a simulation was conducted by varying the gap sizes between the two triboelectric electrodes while holding all other parameters constant and getting the corresponding output voltage. As demonstrated in Fig. 4.8, the excitation intensity was maintained at $0.7g$ while the gap lengths were altered. The bandwidth rises as the gap distance decreases. As the space between frequencies narrows, a wider variety of frequencies will be able to commence impact. However, the output voltage amplitude decreases as the gap distance decreases. Therefore, while choosing the ultimate gap distance, adjustment must be made between the high output voltage and the harvesting of a broad spectrum of energy.

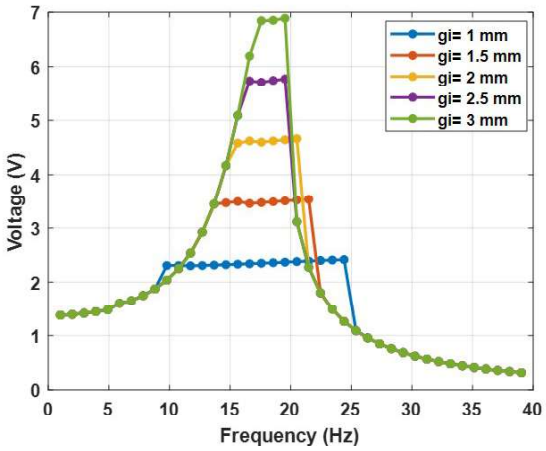

Figure 4.8. The frequency voltage curve at various gap distance g_i, and 15.5 mm separation distance, and at 0.7 g excitation level.

Additionally, the influence of surface charge density was investigated by examining the frequency-voltage response at varying charge densities while holding all other parameters constant ($0.7g$ excitation, $1mm$ gap distance). Fig. 4.9a displays the results of the simulation at various charge densities, and it can be shown that raising the charge density greatly increases the output voltage while having no appreciable influence on the bandwidth. Lastly, the influence of external resistance on the triboelectric circuit was investigated by simulating various external resistance values. Fig. 4.9b depicts the output voltage produced by changing the resistance from $5M$ to $30M$. When the external resistance value increases, the output voltage also increases. It is anticipated that raising the resistance further will raise the voltage output until reaching a point where additional resistance increases will no longer

enhance the output voltage.

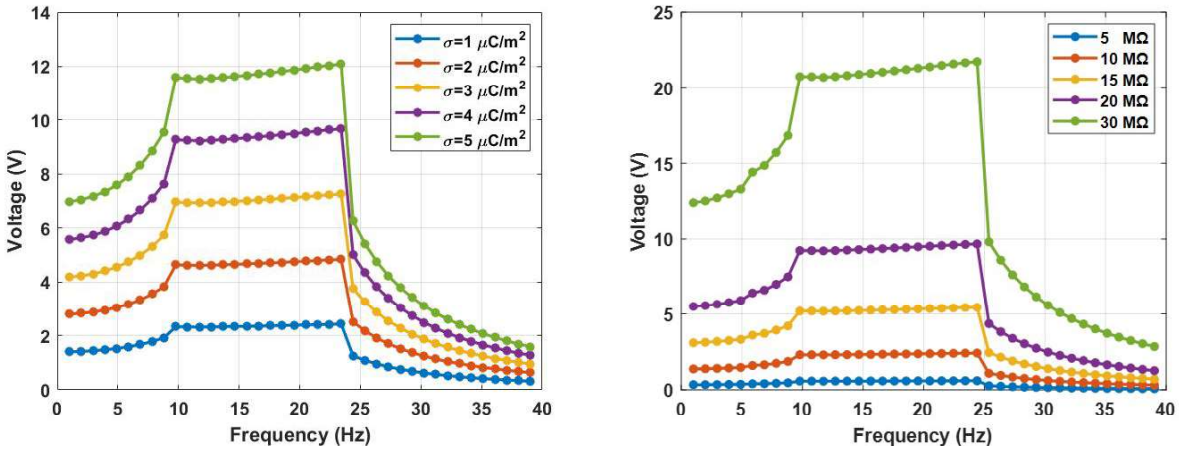

(a) (b)

Figure 4.9. The simulated voltage of the energy harvester under $0.7g$ excitation level and $1mm$ gap distance between the triboelectric layers at different (a) Surface charge densities; (b) External resistance.

Chapter Five

Conclusion

This study describes a method for dramatically improving the performance of triboelectric energy harvesters by combining magnetic nonlinearity and Vibro-Impact for low frequencies. The system comprises a cantilever beam with a tip magnet facing another fixed magnet at the same polarity to create a repulsive magnetic force. Also, a triboelectric energy harvester has been embedded in the system to create a Vibro-impact triboelectric energy harvester. The static and dynamic behavior of the system is examined using a piecewise function lumped parameter model of a single degree of freedom system with a magnetic nonlinearity. The static and frequency variations with separation distance are divided into bistable and monostable regimes by a threshold distance of 9 mm. A nonlinear softening behavior was observed in the monostable and transition region. In contrast, a nonlinear hardening effect dominates in the bistable region. Furthermore, increasing the excitation level induced softening, hardening, and combined behaviors. Combining magnetic nonlinearity with Vibro-Impact produced a greater bandwidth than utilizing them independently, where a 110.41%

increment was achieved compared to the conventional Vipro-impact energy harvester. In addition, employing magnetic nonlinearity, a variable frequency structure has been attained, allowing for a broader range of applications.

References

[1] Paci, D., Schipani, M., Bottarel, V., and Miatton, D., 2008. "Optimization of a piezoelectric energy harvester for environmental broadband vibrations". In 2008 15th IEEE International Conference on Electronics, Circuits and Systems, IEEE, pp. 177–181.

[2] Miller, L. M., Halvorsen, E., Dong, T., and Wright, P. K., 2011. "Modeling and experimental verification of low-frequency mems energy harvesting from ambient vibrations". *Journal of Micromechanics and Microengineering,* ***21***(4), p. 045029.

[3] Vidal, J. V., Slabov, V., Kholkin, A. L., and Dos Santos, M. P. S., 2021. "Hybrid triboelectric-electromagnetic nanogenerators for mechanical energy harvesting: A review". *Nano-Micro Letters,* ***13***(1), pp. 1–58.

[4] Vijayan, K., 2012. "Vibration and shock amplification of drilling tools". PhD thesis, University of Cambridge.

[5] Chen, M., Wang, Z., Zheng, Y., Zhang, Q., He, B., Yang, J., Qi, M., and Wei, L., 2021. "Flexible tactile sensor based on patterned ag-nanofiber electrodes through

electrospinning". *Sensors,* ***21***(7), p. 2413.

[6] Du, T., Zuo, X., Dong, F., Li, S., Mtui, A. E., Zou, Y., Zhang, P., Zhao, J., Zhang, Y., Sun, P., et al., 2021. "A self-powered and highly accurate vibration sensor based on bouncing-ball triboelectric nanogenerator for intelligent ship machinery monitoring". *Micromachines,* ***12***(2), p. 218.

[7] Min, G., Dahiya, A. S., Mulvihill, D. M., and Dahiya, R., 2021. "A wide range self-powered flexible pressure sensor based on triboelectric nanogenerator". In 2021 IEEE International Conference on Flexible and Printable Sensors and Systems (FLEPS), IEEE, pp. 1–4.

[8] Malik, P. S., Abouhawwash, M., Almutairi, A., Singh, R. P., and Singh, Y., 2022. "Comparative analysis of magnetic induction based communication techniques for wireless underground sensor networks". *PeerJ Computer Science,* ***8***, p. e789.

[9] Lin, L., Xie, Y., Wang, S., Wu, W., Niu, S., Wen, X., and Wang, Z. L., 2013. "Triboelectric active sensor array for self-powered static and dynamic pressure detection and tactile imaging". *ACS nano,* ***7***(9), pp. 8266–8274.

[10] Bhatta, T., Maharjan, P., Shrestha, K., Lee, S., Salauddin, M., Rahman, M. T., Rana, S. S., Sharma, S., Park, C., Yoon, S. H., et al., 2022. "A hybrid self-powered arbitrary

wave motion sensing system for real-time wireless marine environment monitoring application". *Advanced Energy Materials,* ***12***(7), p. 2102460.

[11] Zhang, H., Yang, Y., Su, Y., Chen, J., Adams, K., Lee, S., Hu, C., and Wang, Z. L., 2014. "Triboelectric nanogenerator for harvesting vibration energy in full space and as self-powered acceleration sensor". *Advanced Functional Materials,* ***24***(10), pp. 1401–1407.

[12] Wang, Z. L., 2013. "Triboelectric nanogenerators as new energy technology for self-powered systems and as active mechanical and chemical sensors". *ACS nano,* ***7***(11), pp. 9533–9557.

[13] Lin, Z.-H., Zhu, G., Zhou, Y. S., Yang, Y., Bai, P., Chen, J., and Wang, Z. L., 2013. "A self-powered triboelectric nanosensor for mercury ion detection". *Angewandte Chemie International Edition,* ***52***(19), pp. 5065–5069.

[14] Fu, Y., Wang, H., Zi, Y., and Liang, X., 2021. "A multifunctional robotic system toward moveable sensing and energy harvesting". *Nano Energy,* ***89***, p. 106368.

[15] Liu, Y., Chen, B., Li, W., Zu, L., Tang, W., and Wang, Z. L., 2021. "Bioinspired triboelectric soft robot driven by mechanical energy". *Advanced Functional Materials,* ***31***(38), p. 2104770.

[16] Hossain, N. A., Yamomo, G. G., Willing, R., and Towfighian, S., 2021. "Characterization of a packaged triboelectric harvester under simulated gait loading for total knee replacement". *IEEE/ASME Transactions on Mechatronics,* ***26***(6), pp. 2967–2976.

[17] Cottone, F., Vocca, H., and Gammaitoni, L., 2009. "Nonlinear energy harvesting". *Physical Review Letters,* ***102***(8), p. 080601.

[18] Reilly, E. K., Miller, L. M., Fain, R., and Wright, P., 2009. "A study of ambient vibrations for piezoelectric energy conversion". *Proc. PowerMEMS,* ***2009***, pp. 312–315.

[19] Zhu, D., Tudor, M. J., and Beeby, S. P., 2009. "Strategies for increasing the operating frequency range of vibration energy harvesters: a review". *Measurement Science and Technology,* ***21***(2), p. 022001.

[20] Aldraihem, O., and Baz, A., 2011. "Energy harvester with a dynamic magnifier". *Journal of Intelligent Material Systems and Structures,* ***22***(6), pp. 521–530.

[21] Yu, N., Ma, H., Wu, C., Yu, G., and Yan, B., 2021. "Modeling and experimental investigation of a novel bistable two-degree-of-freedom electromagnetic energy harvester". *Mechanical Systems and Signal Processing,* ***156***, p. 107608.

[22] Miao, G., Fang, S., Wang, S., and Zhou, S., 2022. "A low-frequency rotational electromagnetic energy harvester using a magnetic plucking mechanism". *Applied Energy,* ***305***, p. 117838.

[23] Zhao, L.-C., Zou, H.-X., Gao, Q.-H., Yan, G., Liu, F.-R., Tan, T., Wei, K.-X., and Zhang, W.-M., 2019. "Magnetically modulated orbit for human motion energy harvesting". *Applied Physics Letters,* ***115***(26), p. 263902.

[24] Zhou, S., Cao, J., Erturk, A., and Lin, J., 2013. "Enhanced broadband piezoelectric energy harvesting using rotatable magnets". *Applied physics letters,* ***102***(17), p. 173901.

[25] Panda, S., Hajra, S., Mistewicz, K., In-na, P., Sahu, M., Rajaitha, P. M., and Kim, H. J., 2022. "Piezoelectric energy harvesting systems for biomedical applications". *Nano Energy*, p. 107514.

[26] Zhang, Q., Liu, Z., Jiang, X., Peng, Y., Zhu, C., and Li, Z., 2022. "Experimental investigation on performance improvement of cantilever piezoelectric energy harvesters via escapement mechanism from extremely low-frequency excitations". *Sustainable Energy Technologies and Assessments,* ***53***, p. 102591.

[27] Yurchenko, D., Val, D. V., Lai, Z., Gu, G., and Thomson, G., 2017. "Energy harvesting from a de-based dynamic vibro-impact system". *Smart Materials and Structures,* ***26***(10), p. 105001.

[28] Liu, M., Qian, F., Mi, J., and Zuo, L., 2022. "Biomechanical energy harvesting for wearable and mobile devices: State-of-the-art and future directions". *Applied Energy,* ***321***, p. 119379.

[29] Thomson, G., Lai, Z., Val, D. V., and Yurchenko, D., 2019. "Advantages of nonlinear energy harvesting with dielectric elastomers". *Journal of Sound and Vibration,* ***442***, pp. 167–182.

[30] Dhakar, L., Tay, F., and Lee, C., 2015. "Broadband vibration energy harvesting using triboelectric mechanism". In International Conference on Experimental Mechanics 2014, International Society for Optics and Photonics, pp. 93021H–93021H.

[31] Haroun, A., Tarek, M., Mosleh, M., and Ismail, F., 2022. "Recent progress on triboelectric nanogenerators for vibration energy harvesting and vibration sensing". *Nanomaterials,* ***12***(17), p. 2960.

[32] Lin, L., Wang, S., Niu, S., Liu, C., Xie, Y., and Wang, Z. L., 2014. "Noncontact free-rotating disk triboelectric nanogenerator as a sustainable energy harvester and self-powered mechanical sensor". *ACS Applied Materials & Interfaces,* ***6***(4), pp. 3031–3038.

[33] Khandelwal, G., and Dahiya, R., 2022. "Self-powered active sensing based on triboelectric generator". *Advanced Materials*, p. 2200724.

[34] Li, X., Cao, Y., Yu, X., Xu, Y., Yang, Y., Liu, S., Cheng, T., and Wang, Z. L., 2022. "Breeze-driven triboelectric nanogenerator for wind energy harvesting and application in smart agriculture". *Applied Energy,* ***306***, p. 117977.

[35] Jin, C., Kia, D. S., Jones, M., and Towfighian, S., 2016. "On the contact behavior of micro-/nano-structured interface used in vertical-contact-mode triboelectric nanogenerators". *Nano Energy,* ***27***, pp. 68–77.

[36] Rahman, M. T., Rana, S. S., Salauddin, M., Maharjan, P., Bhatta, T., and Park, J. Y., 2020. "Biomechanical energy-driven hybridized generator as a universal portable power source for smart/wearable electronics". *Advanced Energy Materials,* ***10***(12), p. 1903663.

[37] Wang, L., Fei, Z., Qi, Y., Zhang, C., Zhao, L., Jiang, Z., and Maeda, R., 2022. "Overview of human kinetic energy harvesting and application". *ACS Applied Energy Materials.*

[38] Yi, J., Dong, K., Shen, S., Jiang, Y., Peng, X., Ye, C., and Wang, Z. L., 2021. "Fully fabric-based triboelectric nanogenerators as self-powered human–machine interactive keyboards". *Nano-micro letters,* ***13***(1), pp. 1–13.

[39] Zhang, L., Meng, B., Xia, Y., Deng, Z., Dai, H., Hagedorn, P., Peng, Z., and Wang, L., 2020. "Galloping triboelectric nanogenerator for energy harvesting under low wind speed". *Nano Energy,* ***70***, p. 104477.

[40] Ren, Z., Wu, L., Pang, Y., Zhang, W., and Yang, R., 2022. "Strategies for effectively harvesting wind energy based on triboelectric nanogenerators". *Nano Energy*, p. 107522.

[41] Xia, Y., Tian, Y., Zhang, L., Ma, Z., Dai, H., Meng, B., and Peng, Z., 2021. "An optimized flutter-driven triboelectric nanogenerator with a low cut-in wind speed". *Micromachines,* ***12***(4), p. 366.

[42] Wu, C., Huang, H., Li, R., and Fan, C., 2020. "Research on the potential of spherical triboelectric nanogenerator for collecting vibration energy and measuring vibration". *Sensors,* ***20***(4), p. 1063.

[43] Zhao, H., and Ouyang, H., 2021. "Theoretical investigation and experiment of a disc-shaped triboelectric energy harvester with a magnetic bistable mechanism". *Smart Materials and Structures,* ***30***(9), p. 095026.

[44] Zi, Y., Wang, J., Wang, S., Li, S., Wen, Z., Guo, H., and Wang, Z. L., 2016. "Effective energy storage from a triboelectric nanogenerator". *Nature communications,* ***7***.

[45] Yi, F., Lin, L., Niu, S., Yang, P. K., Wang, Z., Chen, J., Zhou, Y., Zi, Y., Wang, J., Liao, Q., et al., 2015. "Stretchable-rubber-based triboelectric nanogenerator and its application as self-powered body motion sensors". *Advanced Functional Materials,* ***25***(24), pp. 3688–3696.

[46] Zhang, X.-S., Han, M.-D., Wang, R.-X., Meng, B., Zhu, F.-Y., Sun, X.-M., Hu, W., Wang, W., Li, Z.-H., and Zhang, H.-X., 2014. "High-performance triboelectric nanogenerator with enhanced energy density based on single-step fluorocarbon plasma treatment". *Nano Energy,* ***4***, pp. 123–131.

[47] Aouali, K., Kacem, N., Bouhaddi, N., Mrabet, E., and Haddar, M., 2020. "Efficient broadband vibration energy harvesting based on tuned non-linearity and energy localization". *Smart Materials and Structures,* ***29***(10), p. 10LT01.

[48] Gibus, D., Gasnier, P., Morel, A., Formosa, F., Charleux, L., Boisseau, S., Pillonnet, G., Berlitz, C. A., Quelen, A., and Badel, A., 2020. "Strongly coupled piezoelectric cantilevers for broadband vibration energy harvesting". *Applied Energy,* ***277***, p. 115518.

[49] Yan, B., Yu, N., Ma, H., and Wu, C., 2022. "A theory for bistable vibration isolators". *Mechanical Systems and Signal Processing,* ***167***, p. 108507.

[50] Fang, S., Chen, K., Xing, J., Zhou, S., and Liao, W.-H., 2021. "Tuned bistable nonlinear energy sink for simultaneously improved vibration suppression and energy harvesting". *International Journal of Mechanical Sciences,* ***212***, p. 106838.

[51] Daqaq, M. F., 2010. "Response of uni-modal duffing-type harvesters to random forced excitations". *Journal of Sound and Vibration,* ***329***(18), pp. 3621–3631.

[52] Rysak, A., and Sedlmayr, M., 2022. "Damping efficiency of the duffing system with additional fractional terms". *Applied Mathematical Modelling,* ***111***, pp. 521–533.

[53] Sebald, G., Kuwano, H., Guyomar, D., and Ducharne, B., 2011. "Experimental duffing oscillator for broadband piezoelectric energy harvesting". *Smart materials and structures,* ***20***(10), p. 102001.

[54] Song, J., Han, X., Zou, Y., Jiang, Y., and Bi, Q., 2022. "Relaxation oscillation patterns induced by amplitude-modulated excitation in the duffing system". *Chaos, Solitons & Fractals,* ***164***, p. 112555.

[55] Dulin, S., Lin, K., Serdukova, L., Kuske, R., and Yurchenko, D., 2022. "Improving the performance of a two-sided vibro-impact energy harvester with asymmetric restitution coefficients". *International Journal of Mechanical Sciences,* ***217***, p. 106983.

[56] Jacquelin, E., Adhikari, S., and Friswell, M. I., 2011. "A piezoelectric device for impact energy harvesting". *Smart Materials and Structures,* ***20***(10), p. 105008.

[57] Afsharfard, A., Shin, H., Hosseini, S., Kim, E. S., Lee, I., and Kim, K. C., 2022. "Design of vibro-impact electromagnetic ocean-wave energy harvesting system; an experimental study". *Ocean Engineering,* ***263***, p. 112168.

[58] Zhang, L., Tang, X., Qin, Z., and Chu, F., 2022. "Vibro-impact energy harvester for low frequency vibration enhanced by acoustic black hole". *Applied Physics Letters,* ***121***(1), p. 013902.

[59] Ibrahim, A., Ramini, A., and Towfighian, S., 2020. "Triboelectric energy harvester with large bandwidth under harmonic and random excitations". *Energy Reports,* ***6***, pp. 2490–2502.

[60] Ibrahim, A., Ramini, A., and Towfighian, S., 2018. "Experimental and theoretical investigation of an impact vibration harvester with triboelectric transduction". *Journal of Sound and Vibration,* ***416***, pp. 111–124.

[61] Rezaei, M., Talebitooti, R., and Liao, W.-H., 2022. "Investigations on magnetic bistable pzt-based absorber for concurrent energy harvesting and vibration mitigation: Numerical and analytical approaches". *Energy,* ***239***, p. 122376.

[62] Ibrahim, A., Towfighian, S., Younis, M., and Su, Q., 2016. "Magnetoelastic beam with extended polymer for low frequency vibration energy harvesting". In SPIE Smart Structures and Materials+ Nondestructive Evaluation and Health Monitoring, International Society for Optics and Photonics, pp. 98060B–98060B.

[63] Ibrahim, A., Towfighian, S., and Younis, M. I., 2017. "Dynamics of transition regime in bistable vibration energy harvesters". *Journal of Vibration and Acoustics,* ***139***(5), p. 051008.

[64] Ibrahim, R. A., 2014. "Recent advances in vibro-impact dynamics and collision of ocean vessels". *Journal of Sound and Vibration,* ***333***(23), pp. 5900–5916.

[65] Cao, D.-X., Xia, W., Guo, X.-Y., and Lai, S.-K., 2021. "Modeling and experiment of vibro-impact vibration energy harvester based on a partial interlayer-separated piezoelectric beam". *Journal of Intelligent Material Systems and Structures,* ***32***(8), pp. 817–831.

[66] Fu, Y., Ouyang, H., and Davis, R. B., 2018. "Nonlinear dynamics and triboelectric energy harvesting from a three-degree-of-freedom vibro-impact oscillator". *Nonlinear Dynamics,* ***92***(4), pp. 1985–2004.

[67] Zhao, C., Hu, G., and Yang, Y., 2022. "A cantilever-type vibro-impact triboelectric energy harvester for wind energy harvesting". *Mechanical Systems and Signal Processing,* ***177***, p. 109185.

[68] Fu, Y., Ouyang, H., and Davis, R. B., 2019. "Triboelectric energy harvesting from the vibro-impact of three cantilevered beams". *Mechanical Systems and Signal Processing,* ***121***, pp. 509–531.

[69] Tan, D., Zhou, J., Wang, K., Cai, C., and Xu, D., 2022. "Modeling and analysis of the friction in a non-linear sliding-mode triboelectric energy harvester". *Acta Mechanica Sinica,* ***38***(4), pp. 1–18.

[70] Zhang, J., and Qin, L., 2019. "A tunable frequency up-conversion wideband piezoelectric vibration energy harvester for low-frequency variable environment using a novel impact- and rope-driven hybrid mechanism". *Applied Energy,* ***240***, pp. 26–34.

[71] Cao, D., Ding, X., Guo, X., and Yao, M., 2021. "Design, simulation and experiment for a vortex-induced vibration energy harvester for low-velocity water flow". *International Journal of Precision Engineering and Manufacturing-Green Technology,* ***8***(4), pp. 1239–1252.

[72] Halim, M. A., and Park, J. Y., 2015. "Piezoceramic based wideband energy harvester using impact-enhanced dynamic magnifier for low frequency vibration". *Ceramics International,* ***41***, pp. S702–S707.

[73] Zhao, L., and Yang, Y., 2018. "An impact-based broadband aeroelastic energy harvester for concurrent wind and base vibration energy harvesting". *Applied Energy,* ***212***, pp. 233–243.

[74] Lai, Z., Wang, J., Zhang, C., Zhang, G., and Yurchenko, D., 2019. "Harvest wind energy from a vibro-impact deg embedded into a bluff body". *Energy Conversion and Management,* ***199***, p. 111993.

[75] Stanton, S. C., McGehee, C. C., and Mann, B. P., 2010. "Nonlinear dynamics for broadband energy harvesting: investigation of a bistable piezoelectric inertial generator". *Physica D: Nonlinear Phenomena,* ***239***(10), pp. 640–653.

[76] Yao, M., Liu, P., Ma, L., Wang, H., and Zhang, W., 2020. "Experimental study on broadband bistable energy harvester with l-shaped piezoelectric cantilever beam". *Acta Mechanica Sinica,* ***36***(3), pp. 557–577.

[77] Fu, Y., Ouyang, H., and Benjamin Davis, R., 2020. "Nonlinear structural dynamics of a new sliding-mode triboelectric energy harvester with multistability". *Nonlinear Dynamics,* ***100***(3), pp. 1941–1962.

[78] Li, H., and Li, A., 2021. "Potential of a vibro-impact nonlinear energy sink for energy harvesting". *Mechanical Systems and Signal Processing,* ***159***, p. 107827.

[79] Zhou, J., Zhao, X., Wang, K., Chang, Y., Xu, D., and Wen, G., 2021. "Bio-inspired bistable piezoelectric vibration energy harvester: Design and experimental investigation". *Energy,* ***228***, p. 120595.

[80] Zhang, W., Liu, Y., and Wu, M., 2019. "Theory and experiment of nonlinear vibrations and dynamic snap-through phenomena for bi-stable asymmetric laminated composite square panels under foundation excitation". *Composite Structures,* ***225***, p. 111140.

[81] Naseer, R., Dai, H., Abdelkefi, A., and Wang, L., 2017. "Piezomagnetoelastic energy harvesting from vortex-induced vibrations using monostable characteristics". *Applied Energy,* ***203***, pp. 142–153.

[82] Harne, R. L., and Wang, K., 2013. "A review of the recent research on vibration energy harvesting via bistable systems". *Smart materials and structures,* ***22***(2), p. 023001.

[83] Drezet, C., Kacem, N., and Bouhaddi, N., 2018. "Design of a nonlinear energy harvester based on high static low dynamic stiffness for low frequency random vibrations". *Sensors and Actuators A: Physical,* ***283***, pp. 54–64.

[84] Costa, L. G., Monteiro, L. L. d. S., Pacheco, P. M. C. L., and Savi, M. A., 2021. "A parametric analysis of the nonlinear dynamics of bistable vibration-based piezoelectric energy harvesters". *Journal of Intelligent Material Systems and Structures,* ***32***(7), pp. 699–723.

[85] Zhu, D., and Beeby, S., 2013. "A broadband electromagnetic energy harvester with a coupled bistable structure". In Journal of Physics: Conference Series, Vol. 476, IOP Publishing, p. 012070.

[86] Arab Hassani, F., Mogan, R. P., Gammad, G. G., Wang, H., Yen, S.-C., Thakor, N. V., and Lee, C., 2018. "Toward self-control systems for neurogenic underactive bladder: a triboelectric nanogenerator sensor integrated with a bistable micro-actuator". *ACS nano,* ***12***(4), pp. 3487–3501.

[87] Deng, H., Ye, J., Du, Y., Zhang, J., Ma, M., and Zhong, X., 2019. "Bistable broadband hybrid generator for ultralow-frequency rectilinear motion". *Nano Energy,* ***65***, p. 103973.

[88] Burgermeister, B., Arnold, M., and Esterl, B., 2006. "Differential-algebraic equations time integration for real-time applications in multi-body dynamics". *ZAMM-Journal of Applied Mathematics and Mechanics/Zeitschrift für Angewandte Mathematik und Mechanik: Applied Mathematics and Mechanics,* ***86***(10), pp. 759–771.

[89] Soliman, M., Abdel-Rahman, E., El-Saadany, E., and Mansour, R., 2008. "A wideband vibration-based energy harvester". *Journal of Micromechanics and Microengineering,* ***18***(11), p. 115021.

[90] Dhakar, L., Liu, H., Tay, F., and Lee, C., 2013. "A new energy harvester design for high power output at low frequencies". *Sensors and Actuators A: Physical,* ***199***, pp. 344–352.

[91] Liu, H., Lee, C., Kobayashi, T., Tay, C. J., and Quan, C., 2012. "Piezoelectric mems-based wideband energy harvesting systems using a frequency-up-conversion cantilever stopper". *Sensors and Actuators A: Physical,* ***186***, pp. 242–248.

[92] Younis, M. I., 2011. *MEMS linear and nonlinear statics and dynamics*, Vol. 20. Springer Science & Business Media.

[93] Zeng, W., Tao, X.-M., Chen, S., Shang, S., Chan, H. L. W., and Choy, S. H., 2013. "Highly durable all-fiber nanogenerator for mechanical energy harvesting". *Energy Environ. Sci.,* ***6***, pp. 2631–2638.

[94] Jin, C., Kia, D. S., Jones, M., and Towfighian, S., 2016. "On the contact behavior of micro-/nano-structured interface used in vertical-contact-mode triboelectric nanogenerators". *Nano Energy,* ***27***, pp. 68–77.